An Arbitrary Lagrangian-Eulerian, coupled neutronics-shock physics model for the analysis of shockwave implosion of solid fissile materials

E. Cervi[a], A. Cammi[a,*]

[a]Politecnico di Milano, Department of Energy, Nuclear Engineering Division, Via La Masa 34, 20156, Milan, Italy

*antonio.cammi@polimi.it

ABSTRACT

The aim of this work is to present a coupled neutronics-shock physics model for the study of shockwave compression of solid fissile materials. The shock-physics solver implements multi-material continuum mechanics balance equations, a hydrodynamic material response model and a dynamic mesh to describe shock-induced deformations in solid bodies. In addition, an Arbitrary Lagrangian-Eulerian (ALE) formulation of the governing equations is adopted, in order to avoid mesh distortion and tangling problems in case of large deformations. As for neutronics, a multigroup SP3 neutron transport model is selected for the estimation of the neutron flux.

Several case studies are presented to validate the developed models, demonstrate the coupling between the two physics and highlight the advantages of the ALE approach.

The proposed model can be a useful tool for the simulation of shock implosion of fissile materials, such as in subcritical plutonium experiments or in reactivity accidents initiated by strong energetic events.

Keywords: Multiphysics; OpenFOAM; Shock physics; Neutronics; Arbitrary Lagrangian-Eulerian.

NOMENCLATURE

Latin symbols

A	Temperature coefficient, m^{-1}
$\boldsymbol{b}$	Body force, kg m^{-2} s^{-2}
c	Precursor density, m^{-3}
e	Internal energy, J kg^{-1}
F_{ALE}	Normalized ALE function, -
f_{ALE}	ALE function, m^{-2} s^{-1}
h	Enthalpy, J kg^{-1}
J_{cell}	Cell Jacobian, -
k	Thermal conductivity, J m^{-1} K^{-1}
k_{eff}	Multiplication factor, -
n	Neutron density, m^{-3}
P_l	Legendre polynomial (l^{th} order)
p	Pressure, Pa
Q	Neutron source, m^{-3} s^{-1}
$\dot{q}$	Power source, J s^{-1} m^{-1}
r_{ALE}	ALE under-relaxation factor, -
T	Temperature, K
t	Time, s
$\boldsymbol{u}$	Material velocity, m s^{-1}
U_S	Lagrangian shock velocity, m s^{-1}
u_S	Eulerian shock velocity, m s^{-1}
V_{cell}	Cell volume, m^3
v	Specific volume, m^3 kg^{-1}
v_o	Specific volume at zero compression, m^3 kg^{-1}
v_i	Neutron velocity, m s^{-1}
$\boldsymbol{w}$	Arbitrary mesh velocity, m s^{-1}
w_{di}	Flight direction weight (S_N), -

Greek symbols

α	Material fraction, -
β	Delayed neutron fraction, -
γ	Grüneisen parameter, -
λ	Precursor decay constant, s^{-1}
$\bar{\mu}$	Average scattering angle cosine, -
$\bar{\nu}$	Average neutrons per fission, -
φ_o	Neutron flux (SP_3), $m^{-2}\,s^{-1}$
φ_2	Second neutron flux moment (SP_3), $m^{-2}\,s^{-1}$
ρ	Density, kg m^{-3}
Σ	Macroscopic cross section m^{-1}
$\underline{\underline{\boldsymbol{\tau}}}$	Stress tensor, Pa
χ	Neutron yield, -
$\boldsymbol{\Omega}$	Flight direction, -

Subscripts

a	Absorption
d	Delayed
ei, ei'	Neutron energy group index (S_N)
di, di'	Flight direction index (S_N)
f	Fission
H	Hugoniot
i, i'	Neutron energy group index (SP_3)
j	j-th material index
k	Delayed neutron precursor group
p	Prompt
r	Removal
sl	Inelastic scattering (l^{th} order)
t	Total
tr	Transport

1. INTRODUCTION

Shock physics is widely studied in many scientific and industrial fields. Knowledge of this subject is employed in the design of conventional and nuclear munitions and to assess their effect. The topic is also of interest in determining high-pressure equations of state needed to study Earth and planets, since shockwaves played an important role in the evolution of the solar system. Shock-induced processes can also be used to produce strongly bonded compacts from powdered materials, such as oxides and nitrides, and to synthesize new chemical compounds (Davison, 2008).

In the nuclear field, knowledge of shock physics is of great importance by virtue of the strong reactivity feedback exerted by pressure waves in fissile materials (Cervi et al., 2018a; Cervi et al., 2019a). Nowadays, this subject is of particular interest to conduct small-scale subcritical experiments using nuclear materials (typically plutonium and enriched uranium) and explosives. In a typical subcritical experiment, a small amount of fissile is imploded by using high-performance charges, strongly increasing its density. However, as opposed to full-scale nuclear weapon tests, no nuclear detonation takes place, since the amount of fissile material is too small to initiate the self-sustaining chain reaction. In this regard, subcritical experiments provide a safe and internationally accepted procedure to obtain actual data about the fissile behavior under extreme pressure conditions (Dillingham, 2016).

In addition, shock physics can also be of interest for nuclear criticality safety applications, i.e., to prevent undesired self-sustained nuclear reactions and to minimize the consequences of this if it were to occur (IAEA Safety Standards, 2014). In particular, strong energetic events, such as chemical explosions, constitute a typical design-basis accident that should be considered due to its potential impact on reactivity (DOE Technical Standard, 2017).

A very important aspect of this topic is the use of computer simulations to study the propagation of shockwaves, the effects they have on materials and the coupling with other physics, such as chemical or nuclear reactions. In this regard, the purpose of the present work is to propose a coupled neutronics-shock physics solver for the analysis of shockwave compression of solid fissile materials. This solver is implemented by

using OpenFOAM (OpenFOAM, 2013), a CFD and multiphysics toolkit based on the finite volume method (Moukalled et al., 2016) for the discretization of high-fidelity partial differential equations. The present model implements multi-material balance equations for mass, momentum and energy, a hydrodynamic material response model and a dynamic mesh, suitable to the describe the deformations of solid materials. Thanks to the multi-material formulation of the governing equations, different equations of state can be selected in different regions of the domain. In addition, an Arbitrary Lagrangian-Eulerian (ALE) algorithm, specifically developed for coupled neutronics-shock physics problems, is implemented, in order to preserve the mesh quality in case of large deformations. Moreover, a multi-group SP_3 neutron transport model is implemented to estimate reactivity and the neutron flux.

Different shock physics codes are currently available (see, e.g., McGlaun and Thompson, 1990; Summers et al., 1997) but, according to present literature, none of them implements a neutronics solver. On the other hand, a coupling between a Monte Carlo code and a thermal-mechanics model has been proposed by (Aufiero et al., 2015), but it implements a Lagrangian moving mesh and a linear thermo-elastic material response model, suitable for simulating only small deformations. The aim of this work is to fill this gap, presenting a multiphysics solver that inherently couples neutron transport and shock physics in the same simulation environment, without requiring the development of external interfaces between different, dedicated codes. In fact, the adoption of coupling interfaces can be inefficient for strongly non-linear problems (Ragusa and Mahadevan, 2009; Mahadevan et al., 2012), time-expensive and potentially prone to coding errors.

The proposed solver can be a useful tool to support the design of subcritical experiments and to assess their safety, as well as to study reactivity accidents initiated by chemical explosions or high velocity impact events. However, the analysis of real-life scenarios is not in the scope of the present work, as focus is placed on the model development, verification and validation.

The remainder of this paper is organized as follows. In Section 2, the solver structure, the neutronics and the shock physics models are presented. In Section 3, the shock physics model is validated against experimental Hugoniot curves. In Section 4, the neutronics model is validated by simulating a Godiva super-prompt-critical burst and comparing the results to experimental data, theoretical calculations and a Monte Carlo simulation. In Section 5, two case studies are selected to demonstrate the coupling between the two physics and the capability of the proposed solver to describe both subcritical and supercritical scenarios. The impact of the system geometry on reactivity during the implosion is also highlighted. In Section 6, an ALE algorithm, developed to study imploding fissile bodies, is presented, highlighting its advantages compared to a purely Lagrangian approach. Conclusions and future research perspectives are discussed in Section 7. In addition, in Appendix A, a discrete-ordinate neutron transport model is introduced, highlighting its improvements with respect to the SP_3 model presented in Section 2.

2. THE MODELLING APPROACH

In this section, the structure of the solver and the multi-physics coupling strategy are described. At each time step, thermal-mechanics and neutronics are solved in two different iterative cycles, as shown in Fig. 1. At the beginning of the time step, the thermal-mechanics cycle solves the material fraction, continuity, momentum and energy equations and the equation of state, determining the material density, velocity, the mechanical stresses and temperature. Picard iterations are performed until the thermal-mechanics solution converges. Once material velocity is known, the solid particle displacement in that time step is calculated and the mesh is deformed accordingly, using the ALE algorithm. Then, the neutronics cycle begins, updating the cross sections according to the temperature and density calculated by the thermal-mechanics model and solving iteratively for the neutron flux and for the delayed neutron precursor densities, until convergence is achieved. The power density distribution is then evaluated, in order to update the energy equation in the following thermal-mechanics cycle.

A certain number of external iterations between the thermal-mechanics and the neutronics solvers are performed. The external iterations are particularly important in fast, non-linear transients, when the characteristic times of neutronics and thermal-mechanics are comparable (this is the case in coupled neutronics-shock physics problems).

Summarizing, the following information is exchanged between the two sub-solvers. The fuel temperature and density are passed from thermal-mechanics to neutronics, in order to evaluate the cross sections. On the other hand, the power density distribution is passed from the neutronics to the thermal-mechanics solver, in order to update the energy balance. Finally, once convergence is reached for the coupled neutronics and thermal-mechanics solution, the solver proceeds to the next time step.

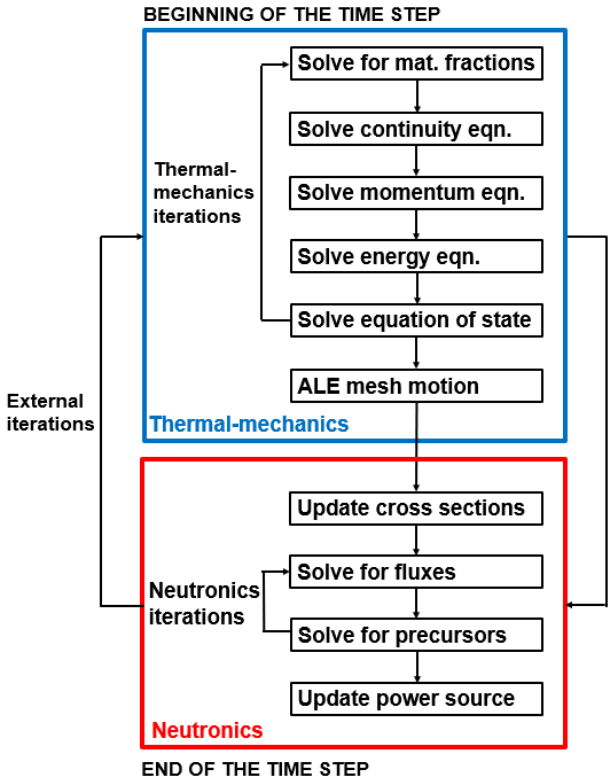

Figure 1. Solver structure and coupling strategy.

2.1. The shock physics module

The continuum evolution equations for multi-material thermal-mechanics are (Robinson et al., 2008):

1. Conservation of material fractions:

$$\frac{\partial \alpha_j}{\partial t} + (\boldsymbol{u} - \boldsymbol{w}) \cdot \nabla \alpha_j = 0 \quad with\, j = 1, \dots, N_{materials} \tag{1}$$

2. Conservation of mass:

$$\frac{\partial \alpha_j \rho_j}{\partial t} + \nabla \cdot \left[\alpha_j \rho_j (\boldsymbol{u} - \boldsymbol{w})\right] = 0 \tag{2}$$

3. Conservation of momentum:

$$\frac{\partial (\rho \boldsymbol{u})}{\partial t} + \nabla \cdot [\rho \boldsymbol{u} (\boldsymbol{u} - \boldsymbol{w})] = \nabla \cdot \underline{\underline{\boldsymbol{\tau}}} - \nabla p + \boldsymbol{b} \tag{3}$$

4. Conservation of total enthalpy:

$$\frac{\partial (\rho h)}{\partial t} + \nabla \cdot [\rho h (\boldsymbol{u} - \boldsymbol{w})] = k \nabla^2 T + \frac{Dp}{Dt} + \dot{q} \tag{4}$$

where the global density ρ is defined as:

$$\rho = \sum_{j=1}^{N_{materials}} \alpha_j \, \rho_j \tag{5}$$

Thanks to the multi-material formulation of the governing equations, different material models can be adopted in different regions of the domain. Presently, different equations of state are implemented into the solver (e.g., perfect gas, linearly compressible liquid, linear thermo-elastic solid). This paper will focus on the development and validation of a hydrodynamic model, based on the Mie-Grüneisen equation of state for the description of strong shockwave propagation in solids (see Section 2.1.1).

Once Eqs. (1) to (4) are solved, the dynamic mesh is moved in order to describe the material deformations. More specifically, the solid particle displacement is calculated at the centroids of the mesh cells and is interpolated to the mesh vertices, which are moved accordingly.

The balance equations are written in an Arbitrary Lagrangian-Eulerian (ALE) form (Hirt et al., 1974): the mesh vertices can be moved with an arbitrary velocity $\boldsymbol{w}$, to preserve the mesh quality in case of strong distortions and/or tangling issues. In typical ALE approaches $w \geq 0$ and $w < u$. The velocity $\boldsymbol{w}$ is included in the advective terms of the equations in order to preserve the balances. Different high-resolution schemes are already implemented in the OpenFOAM toolkit for the discretization of the divergence operator in hyperbolic problems and to flux each physical quantity between different cells (LeVeque, 2002; Moukalled et al., 2016).

In more detail, if $\boldsymbol{w}$ is set to be equal to $\boldsymbol{u}$, the equations are reduced to a purely Lagrangian form, in which the mesh follows the motion of the solid particles. Lagrangian approaches are generally more accurate, allowing an easier tracking of free surfaces or material interfaces. This is particularly important in neutronics simulations, in which the deformation of the material boundary affects neutron leakages, having a significant impact on reactivity. However, in case of strong deformations, Lagrangian approaches may suffer from mesh tangling and distortion problems which can make the problem incomputable. On the other hand, setting $\boldsymbol{w} = 0$, a purely Eulerian approach is obtained. Eulerian approaches are not affected by mesh distortion problems, since the mesh is fixed through the entire simulation, but they are generally less accurate due to numerical diffusion and dispersion, resulting in a lower resolution of the flow details.

To overcome the issues of purely Lagrangian and Eulerian descriptions, ALE techniques have been developed to combine the best feature of both the approaches (Hirt et al., 1974). Thanks to the freedom in moving the mesh offered by the ALE approach, large distortions can be handled, while preserving the accurate description of interfaces typical of a purely Lagrangian approach. Many ALE algorithms are available in literature, which adopt different criteria to determine the arbitrary mesh velocity (Donea et al., 2004). In Section 6, a new algorithm, specifically developed for coupled neutronics-shock physics problems, is presented.

Finally, a constitutive relation is also required to close the thermal-mechanics problem, in addition to Eqs. (1) to (5). To this aim, a material response model for strong shockwave compression of solids is presented in the next subsection.

2.1.1. The hydrodynamic model

A shockwave is a very thin region of rapid state variation across which there is a flow of matter (Thompson, 1972). For most application, this region is so thin that it can be modelled as a surface discontinuity in space (Fig. 2).

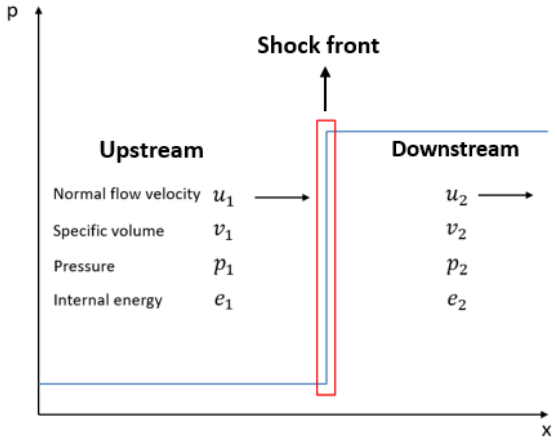

Figure 2. Structure of a shockwave (the horizontal black arrows indicate the matter flow direction with respect to the shock front).

The numerical simulation of shock propagation in a solid medium is a challenging task, requiring the implementation of different material response models, depending on the strength of a given shock. In more details, finite-strain, high-strain-rate plasticity models are required to describe shock-induced material deformations. In general, these models are extremely complex both from a theoretical and numerical point of view.

However, above very high pressures of 5-10 GPa, the description of the shock propagation phenomenon greatly simplifies, since shear stresses become negligible and the solid response to shock compression becomes similar to that of an inviscid, compressible fluid (Davison, 2008). This is known as the *hydrodynamic approximation.*

Within this approximation, the *"shock conditions"*, expressing integral mass, momentum and energy balance across the shock front, become:

$$[\rho]u_s = [\rho u] \tag{6}$$

$$[\rho u]u_s = [\rho u^2 + p] \tag{7}$$

$$\left[\rho\left(e + \frac{1}{2}u^2\right)\right]u_s = \left[\rho\left(e + \frac{1}{2}u^2\right)u + pu\right] \tag{8}$$

where the notation [] indicates the difference between the upstream and downstream conditions with respect to the shock front, while u_s is the Eulerian shock velocity. Elaborating Eqs. (7) and (8), the important Rankine-Hugoniot relation can be derived:

$$e_2 - e_1 = \frac{1}{2}(p_1 + p_2)(v_1 - v_2) \tag{9}$$

where the indices 1 and 2 indicate the upstream and downstream conditions, respectively (see Fig. 2).

Finally, combining Eq. (9) with an equation of state $e = f(p, v)$, the Hugoniot curve, or *shock adiabat*, can be obtained, which relates the initial and the possible final states of a material crossed by a shockwave. Thanks to the shock conditions, the Hugoniot curve can be expressed in different forms. Among these, the $u - U_s$ (material velocity – Lagrangian shock velocity) curve is one of the most commonly used to represent experimental data. Above pressures of 5-10 GPa, the $u - U_s$ Hugoniot assumes a simple linear form:

$$U_s = C_B + S[u] \tag{10}$$

where C_B and S are material constants. In more details, C_B represent the bulk speed of sound and strongly varies depending on the material, while the linear coefficient S has typical values of about 1.5 (Davison 2008).

Moreover, when the hydrodynamic approximation holds, a solid can be described with the $p - v - e$ Mie-Grüneisen equation of state (Davison, 2008, p. 100):

$$p - p_H = \frac{\gamma(v)}{v}(e - e_H) \tag{11}$$

where p_H and e_H are the pressure and internal energy lying on a Hugoniot curve, while γ is the Grüneisen parameter. Once C_B and S are known from experimental measurements, p_H and e_H can be determined using the shock conditions and several algebraic manipulations. On the other hand, the Grüneisen parameter can be estimated as (Grodzka, 1967):

$$\gamma(v) = \left(\frac{v}{v_0} - 1\right)\left(S^2 - \frac{1}{3}S + \frac{5}{9}\right) + (2S - 1) \tag{12}$$

Therefore, C_B and S are the input parameters required by the model to write the Mie-Grüneisen equation of state, closing the thermal-mechanics problem. If these parameters are known, p_H, e_H and γ can be determined and the propagation of a shockwave in a solid material can be described.

2.2. The neutronics module

A multi-group SP_3 transport model (Cervi et al., 2018b; Cervi et al., 2018c; Cervi et al., 2019b; Cervi et al., 2019c), with a user-selectable number of energy groups, is adopted for the estimation of the neutron flux. Compared to diffusion approaches, a transport model is more suitable for the description of small systems, in which neutron leakages have a strong feedback on reactivity (Stacey, 2007). At the same time, the SP_3 approach is characterized by lower computational requirements compared to more accurate neutronics models (e.g., S_N or integral approaches), being therefore suitable for complex multiphysics simulations. In this regard, the SP_3 equations are selected as a trade-off between model accuracy and computational cost (Brantley and Larsen, 2000):

$$\frac{1}{v_i}\frac{\partial \Phi_{0,i}}{\partial t} = \nabla \cdot D_{0,i}\nabla\Phi_{0,i} - \Sigma_{r,i}\left(\Phi_{0,i} - 2\varphi_{2,i}\right) + S_n(1-\beta)\chi_{p,i} + S_d\chi_{d,i} + S_{s,i} + \frac{2}{v_i}\frac{\partial \varphi_{2,i}}{\partial t} \tag{13}$$

$$\begin{aligned}\frac{9}{5}\frac{1}{v_i}\frac{\partial \varphi_{2,i}}{\partial t} = {} & \nabla \cdot D_{2,i}\nabla\varphi_{2,i} - \Sigma_{t2,i}\varphi_{2,i} + \frac{2}{5}\Sigma_{r,i}\left(\Phi_{0,i} - 2\varphi_{2,i}\right) \\ & -\frac{2}{5}S_n(1-\beta)\chi_{p,i} - \frac{2}{5}S_d\chi_{d,i} - \frac{2}{5}S_{s,i} + \frac{2}{5}\frac{1}{v_i}\frac{\partial \Phi_{0,i}}{\partial t}\end{aligned} \tag{14}$$

Where the removal cross section $\Sigma_{r,i} = \Sigma_{a,i} + \sum_{i'\neq i}^{energy\ groups}\Sigma_{s,i\to i'}$, while S_n, $S_{s,i}$ and S_d are the fission neutron, scattering neutron and delayed neutron source terms, respectively:

$$S_n = \sum_{i'}^{energy\ groups} \bar{\nu}\Sigma_{f,i'}\varphi_{0,i'} \tag{15}$$

$$S_{s,i} = \sum_{i'\neq i}^{energy\ groups} \Sigma_{s,i'\to i}\varphi_{0,i'} \tag{16}$$

$$S_d = \sum_{k}^{prec.\ groups} \lambda_k c_k \tag{17}$$

while:

$$\Phi_{0,i} = \varphi_{0,i} + 2\varphi_{2,i} \tag{18}$$

$$D_{0,i} = \frac{1}{3\Sigma_{tr,i}} \tag{19}$$

$$\Sigma_{t2,i} = \Sigma_{t,i} - \Sigma_{s2,i\to i} \tag{20}$$

$$D_{2,i} = \frac{9}{35}\frac{1}{\Sigma_{t,i} - \Sigma_{s3,i\to i}} \tag{21}$$

The transport cross section appearing in Eq. (19) is defined as $\Sigma_{tr,i} = \Sigma_{s,i\to i}(1-\bar{\mu})$, where $\bar{\mu}$ is the average cosine of the scattering angle in the laboratory coordinate system, and its value is calculated by Monte Carlo simulation.

Cross sections are evaluated by assuming a logarithmic dependence on temperature and a linear dependence on density (even if different relationships can be easily implemented into the solver):

$$\Sigma_{[reaction],i} = \left[\Sigma^{o}_{[reaction],i} + A_{[reaction],i} log\frac{T}{T_{ref}}\right]\frac{\rho}{\rho_{ref}} \tag{22}$$

where the reference term $\Sigma^{o}_{[reaction],i}$ is a group-constant cross section evaluated by Monte Carlo simulation at reference temperature T_{ref} and density ρ_{ref}, while $A_{[reaction],i}$ is calculated by logarithmic interpolation of two cross sections values, obtained at T_{ref} and at a different temperature (always by Monte Carlo simulation).

Balance equations for precursor densities are implemented into the neutronics model:

$$\frac{\partial c_k}{\partial t} + \nabla \cdot [c_k(\boldsymbol{u} - \boldsymbol{w})] = \beta_k \sum_{i=1}^{energy\ groups} \bar{\nu}\Sigma_{f,i}\varphi_i - \lambda_k c_k \tag{23}$$

A power iteration routine, based on the *k*-eigenvalue method (Bell and Glasstone, 1970), is also implemented for the estimation of the multiplication factor. For more details the reader is referred to (Cervi et al., 2017). In appendix A, the potential limits of the SP_3 equations are discussed and a more advanced, discrete-ordinate neutron transport model is presented.

2.3. Details on the solution algorithm and on the treatment of non-linear terms

In this section, the solution algorithm presented in Fig. 1 is described in more detail (see Fig. 3).

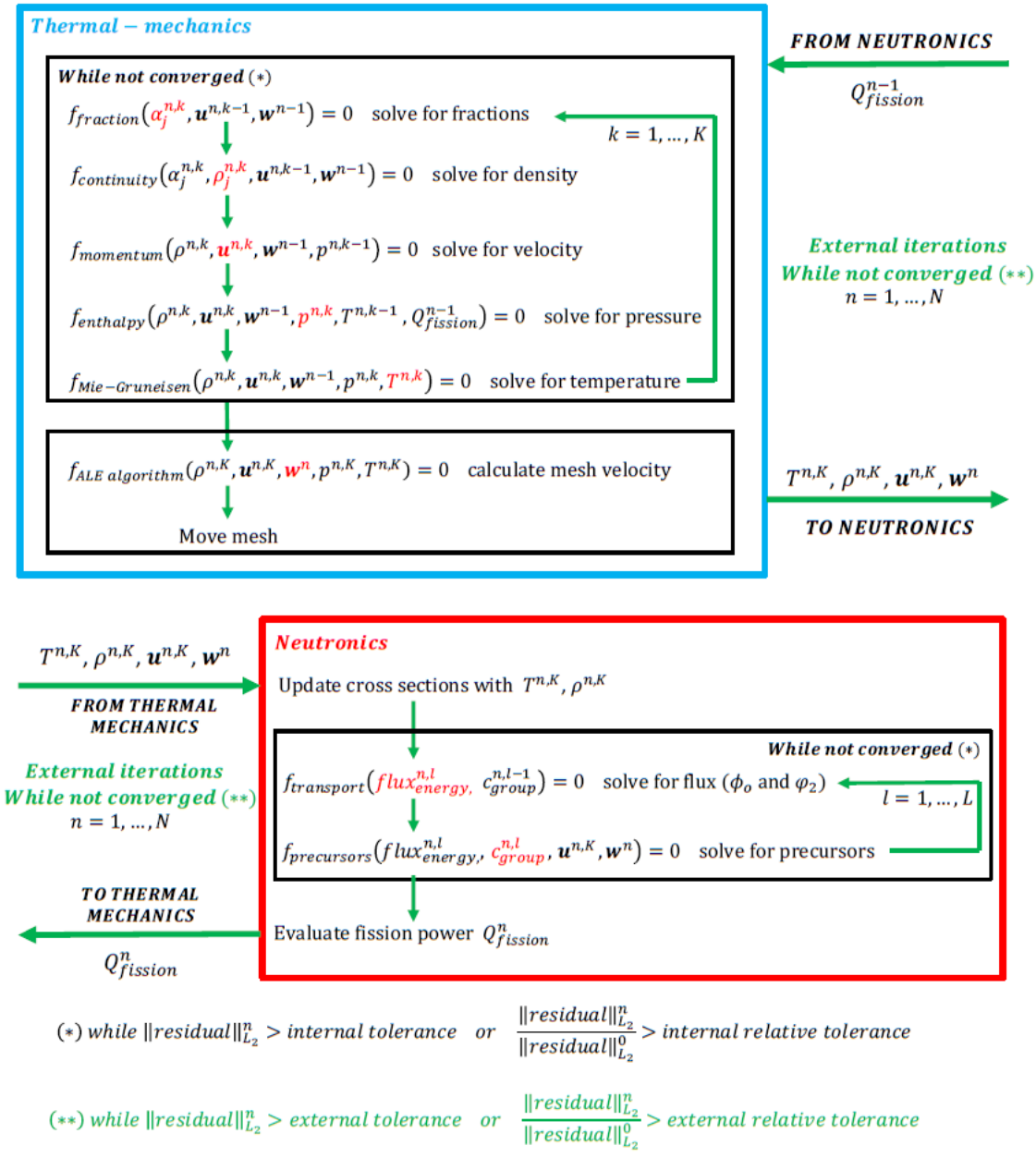

Figure 3. The treatment of non-linearities: thermal-mechanics (top) and neutronics (bottom).

The implicit treatment of the non-linear terms within each physics is handled by adopting a segregated, iterative solver. Each equation is solved separately from the others for a specific variable as indicated by Fig. 3, and Picard iterations are performed to ensure convergence. Consistently with this solution algorithm, the divergence term of the momentum equation, $\nabla \cdot [\rho \boldsymbol{u}(\boldsymbol{u}-\boldsymbol{w})]$, is linearized as $\nabla \cdot \left[\rho^{n,k}\boldsymbol{u}^{n,k-1}\left(\boldsymbol{u}^{n,k}-\boldsymbol{w}^{n-1}\right)\right]$ and the momentum equation is solved for $\boldsymbol{u}^{n,k}$. It is worth noting that pressure is evaluated from the enthalpy balance equation, while temperature from the equation of state. This is a difference with respect to typical density-based solvers, in which the continuity equation is solved for density, the momentum equation for velocity, the energy equation for temperature and the equation of state for pressure (Moukalled et al., 2016). This choice is justified by the fact that with strong shockwaves, the pressure contribution to enthalpy is much larger than the temperature one. After several testing, this formulation proved to yield more accurate results, compared to typical density-based and pressure-based solvers.

The adoption of a Picard solver implies that the time step Δt must satisfy the condition $U_s \Delta t \ / \Delta x_{min} \leq 1$, where Δx_{min} is the minimum cell dimension in the computational domain. For all the case studies presented in the remainder of the paper, temporal convergence studies - not shown for the sake of brevity - have been carried out, verifying that once this condition is met, the solution is not significantly modified by further time-step refinements.

3. VALIDATION OF THE SHOCK PHYSICS MODULE

In this section, the hydrodynamic model developed for shock physics analysis is validated against the experimental Hugoniot curves of different metallic materials. In particular, the Lagrangian shock speed calculated by the proposed solver is compared to that predicted by the experimental curves for different strength one-dimensional shockwaves. This test is also useful to verify the spatial stability of the shock profiles, as it is well known that numerical oscillations can often be an issue in the numerical simulation of shockwave propagation (LeVeque, 2002).

To this purpose, the propagation of different strength one-dimensional shocks is simulated in a semi-infinite solid medium. At the initial time $t = 0$, a pressure step is applied to the surface of the medium, at $x = 0$ (see Fig. 4). The resulting shockwave propagates through the solid with a velocity that depends both on the material properties, through the Hugoniot curve Eq. (10), and on the applied pressure, through the shock conditions Eqs. (6) to (8). A one-dimensional moving mesh is adopted to describe shock-induced material deformations. In this section, a purely Lagrangian approach is adopted, since the considered case study is not affected by mesh tangling and distortions issues.

Simulations are carried out choosing four different materials, i.e., uranium, plutonium, aluminium and copper. The main thermo-mechanical parameters of interest for the present calculations are listed in Tab. I (Isbell et al., 1971; Davison, 2008).

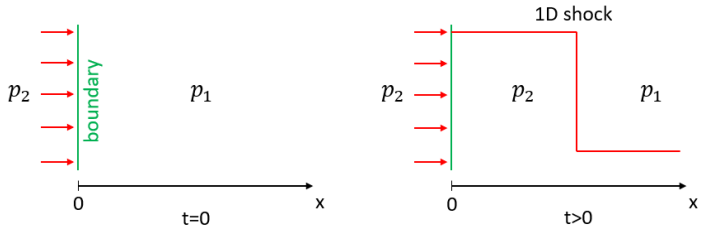

Figure 4. Simulation of one-dimensional shockwaves.

Table I. Thermophysical properties and parameters adopted for the present analysis.

	ρ_0 (kg m^{-3})	C_B (m/s)	S (-)	c_p (J kg^{-1} K^{-1})
Uranium	18951	2487	1.539	117
Plutonium	19800	1651	1.5 (assumed)	113
Aluminum	2785	5328	1.338	875
Copper	8930	3940	1.489	386

For each material, different strength shockwaves, from 10 to 100 GPa, are simulated. For each case, the Lagrangian shock speed is calculated by post-processing the output of the simulation. Then, the outcome is compared to the value predicted by the $U_s - u$ Hugoniot curve in correspondence of the material velocity u calculated by the solver. Results are presented in Tables II to V.

Table II. Shock speeds calculated by the solver and by the experimental Hugoniot curve for uranium.

Pressure (GPa)	Calculated shock speed (m/s)	Shock speed from Hugoniot (m/s)	Relative error (%)
10	2766	2779	-0.47
20	3000	3024	-0.79
30	3208	3239	-0.96
40	3437	3433	0.12
50	3588	3611	-0.64
60	3738	3777	-1.03
70	3886	3932	-1.17
80	3988	4045	-1.41
90	4131	4183	-1.24
100	4260	4313	-1.23

Table III. Shock speeds calculated by the solver and by the experimental Hugoniot curve for plutonium.

Pressure (GPa)	Calculated shock speed (m/s)	Shock speed from Hugoniot (m/s)	Relative error (%)
10	1973	2013	-1.99
20	2256	2289	-1.44
30	2486	2523	-1.47
40	2703	2728	-0.92
50	2891	2913	-0.76
60	3037	3080	-1.40
70	3194	3234	-1.24
80	3348	3379	-0.92
90	3481	3516	-1.00
100	3610	3643	-0.91

Table IV. Shock speeds calculated by the solver and by the experimental Hugoniot curve for aluminum.

Pressure (GPa)	Calculated shock speed (m/s)	Shock speed from Hugoniot (m/s)	Relative error (%)
10	6088	6114	-0.43
20	6722	6751	-0.43
30	7158	7302	-1.97
40	7692	7793	-1.30
50	8087	8242	-1.88
60	8621	8657	-0.42
70	8971	9045	-0.82
80	9308	9410	-1.08
90	9651	9757	-1.09
100	9978	10088	-1.09

Table V. Shock speeds calculated by the solver and by the experimental Hugoniot curve for copper.

Pressure (GPa)	Calculated shock speed (m/s)	Shock speed from Hugoniot (m/s)	Relative error (%)
10	4300	4326	-0.60
20	4665	4656	0.19
30	4963	4951	0.24
40	5199	5218	-0.36
50	5418	5465	-0.86
60	5630	5696	-1.16
70	5830	5913	-1.40
80	6044	6119	-1.23
90	6229	6316	-1.38
100	6426	6503	-1.18

3.1. Discussion of results

The relative error between the computed and the experimental speeds remains below 2% over the entire investigated pressure range and for all the considered materials. It is interesting to note that errors do not increase at higher pressure values. According to the authors, this is because pressure, instead of temperature, is evaluated from the enthalpy balance equation, improving the model accuracy. It is recalled that this choice is made because with very strong shockwaves the pressure contribution to enthalpy is larger than the temperature one (see Section 2.3). After several testing, it was observed that this trend could not be reproduced with any other density or pressure-based formulations of the solver.

The validity of the shock conditions Eqs. (6) to (8) has been verified for each case, ensuring that the calculated shock speeds are coherent to the pressure, material velocity, density and temperature profiles. These profiles are presented in Figs. 5 and 6, for 100 GPa shockwaves travelling in uranium and plutonium, respectively. Despite the very high pressure, no significant unphysical oscillation is observed.

In this regard, the proposed model proves to be accurate and numerically stable, constituting a promising tool for the analysis of strong dynamic compression of solid materials. Even more so, the good performance of the model at describing shock propagation in uranium and plutonium makes it suitable to the simulation of coupled neutronics and shock physics problems.

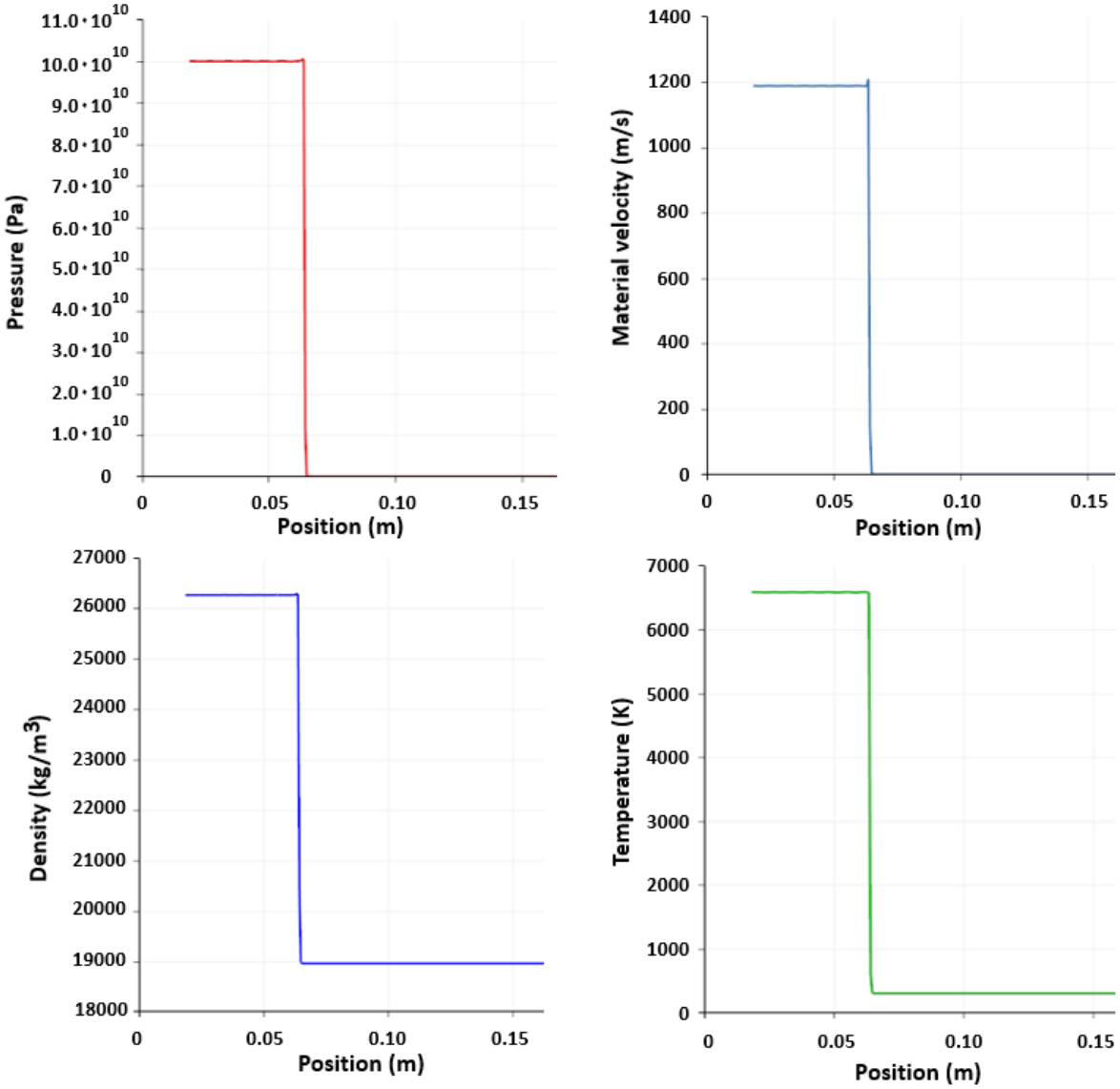

Figure 5. Pressure, material velocity, density and temperature profiles in the 100 GPa case in uranium at time instant $t = 15\ \mu s$.

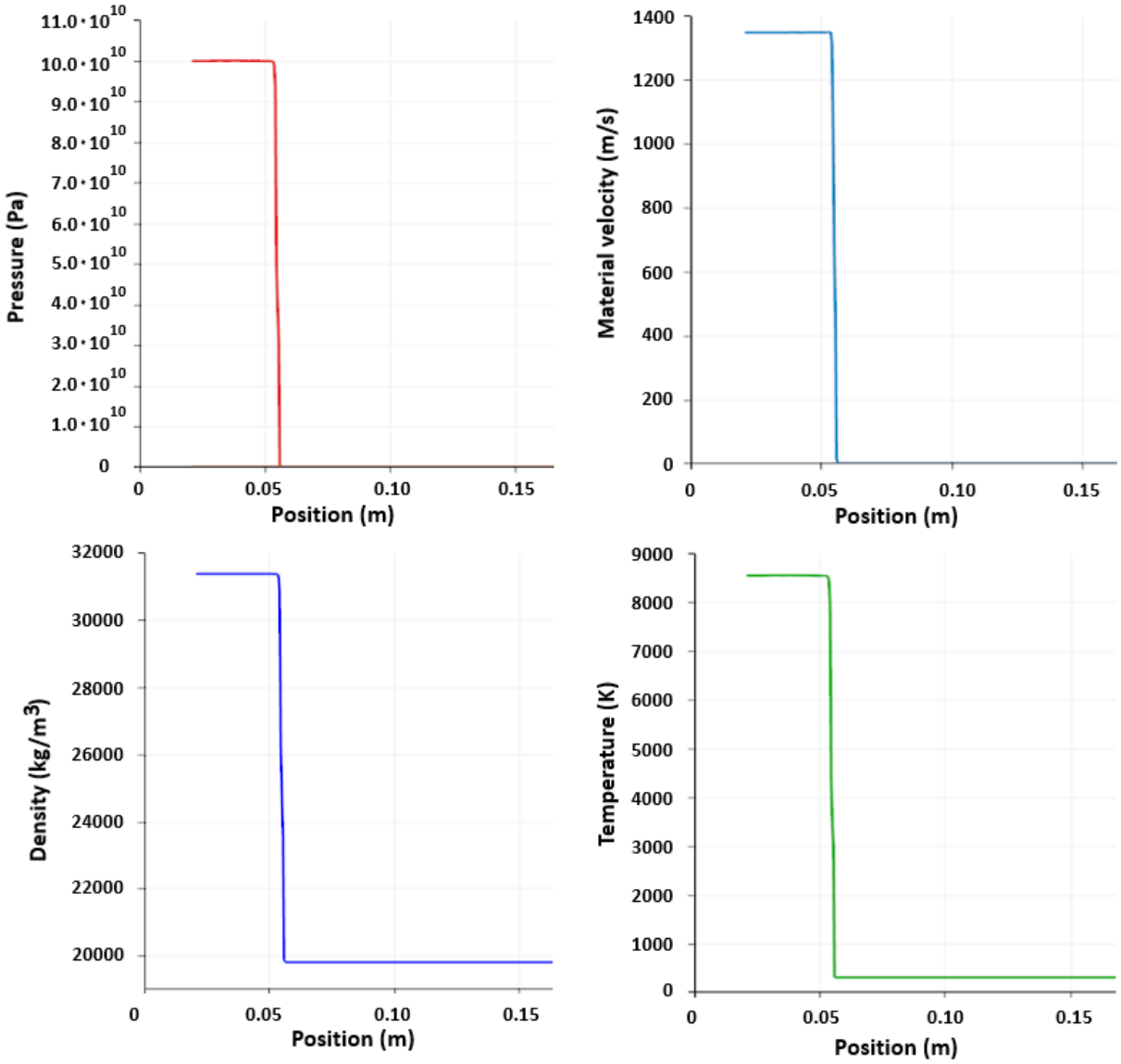

Figure 6. Pressure, material velocity, density and temperature profiles in the 100 GPa case in plutonium at time instant $t = 15\ \mu s$.

4. VALIDATION OF THE NEUTRONICS MODULE: THE GODIVA TEST CASE

In this Section, the neutronics model is validated against a Godiva super-prompt-critical burst. The predictions of the proposed model are compared to experimental data, analytical calculations (Wimett, 1956) and a simulation carried out by (Aufiero et al., 2015) by coupling the Monte Carlo code Serpent 2 (Leppänen et al, 2015) and an OpenFOAM thermal-mechanics solver. Instead of the Mie-Grüneisen equation of state presented in Section 2.1.1, a simpler linear thermo-elastic material response model is adopted to describe the thermal expansion of the Godiva sphere. This constitutive model is not shown for brevity, and for more details the reader is referred to (Fung and Tong, 2001). A purely Lagrangian description is selected for this case study, as thermal expansion is very small and mesh distortion is not an issue in this simulation.

Lady Godiva was an unshielded, metallic uranium reactor, built at Los Alamos National Laboratory (Wimett, 1956). It was fabricated by three sections that go together to form a sphere (see Fig. 7). The assembly has a critical mass of about 54 kg of uranium enriched to about 90% atomic abundance in ^{235}U, and a diameter of about 17.1 cm. Godiva was employed as a pulsed reactor, by sudden establishment of super-prompt-critical conditions starting from a negligible initial neutron population. Results of these experiments served to demonstrate the self-limitation of fission energy release by thermal expansion in fast reactors. Following an initial exponential increase, the observed fission rate reaches a bell-shaped maximum, or “burst”, due to the reactivity decrease from thermal expansion, which increases neutron leakages from the reactor boundary. In this regard, the Godiva test case is useful to assess the accuracy of the neutronics model, especially in small,

leakage-dominated systems and to verify the capability of the moving mesh to correctly describe the thermal expansions feedbacks that determine the system dynamics.

A super-prompt-critical transient with initial reactor period 29.5 μs (corresponding to 32 pcm above the super-prompt-critical) is selected for this analysis. Due to the short duration of the burst, the reactor boundary is assumed to be adiabatic, since the transient characteristic times are too small for convection to cool down the system. Following this assumption, all the energy released by fission remains in the system without being dissipated to the external environment. Homogenised cross sections are calculated from a Serpent 2 model of Godiva, using the JEFF-3.1.1. nuclear data library (Santamarina et al., 2009). Even if an arbitrary number of neutron energy groups can be selected in the SP_3 model, only one group is adopted for the sake of simplicity. Due to the high ^{235}U enrichment, the Doppler effect is negligible, as also observed by (Aufiero et al., 2015). This can be easily verified by performing Monte Carlo simulations of the Godiva sphere at different temperatures. Consequently, the temperature coefficient $A_{absorption,i}$ - see Eq. (22) - is set to zero (note that the absorption contribution appears in the definition of the removal cross section, as discussed in Section 2.2). The main parameters assumed in the burst simulation are listed in Tab. VI (Aufiero et al., 2015).

A comparison between the solver prediction, experimental data and theoretical results (obtained with a point kinetics model) is shown in Fig. 8. The original picture is reported from (Wimett, 1956) and represents two different pulses with reactor periods of 29.5 and 320 μs, respectively. In this work, only the 29.5 μs transient is simulated and compared.

Moreover, the calculated, theoretical and experimental peak fission rates are compared in Tab. VII, while Fig. 9 shows the neutron flux, temperature, material density and displacement fields at the time instant of the fission rate peak.

Figure 7. The Lady Godiva reactor.

Table VI. Parameters assumes in this work.

Density (ρ)	18740	$kg\ m^{-3}$
Poisson's ratio (ν)	0.23	-
Young's modulus (E)	208	GPa
Thermal conductivity (k)	27.5	$W\ m^{-1}K^{-1}$
Thermal expansion coefficient (α_{th})	$1.39{\cdot}10^{5}$	K^{-1}
Specific heat (c)	117.72	$J\ kg^{-1}K^{-1}$

Table VII. Calculated, theoretical and experimental peak fission rate.

	Absolute value (s^{-1})	Relative error with respect to the experimental peak (%)
OpenFOAM	$2.69{\cdot}10^{20}$	0.75
Theoretical	$2.68{\cdot}10^{20}$	0.37
Experimental	$2.67{\cdot}10^{20}$	-

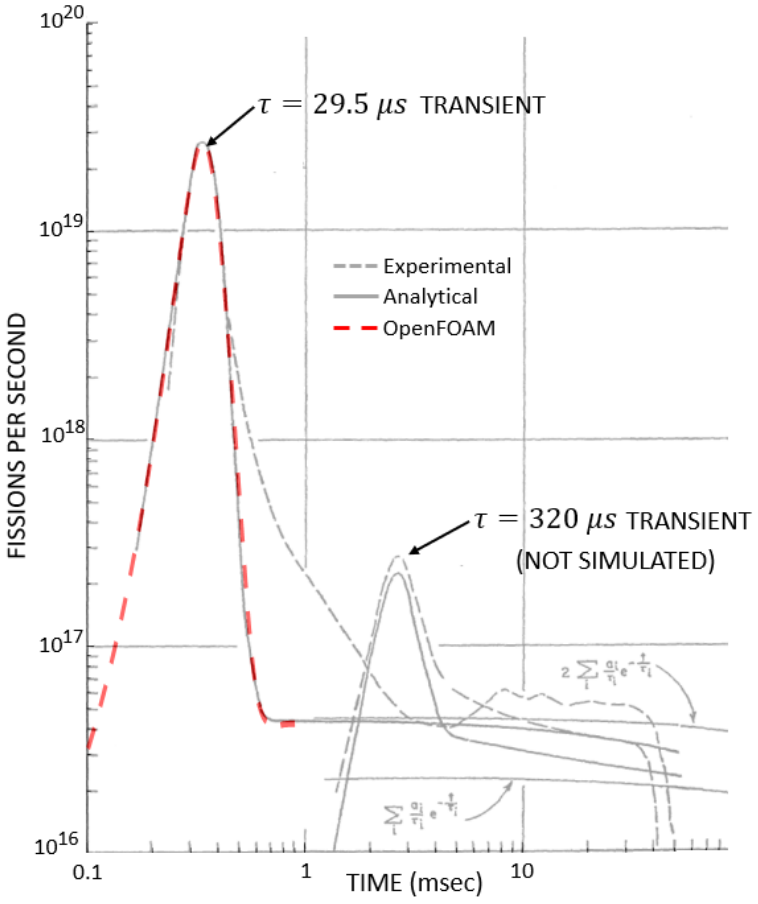

Figure 8. Godiva super-prompt-critical burst: OpenFOAM (red dashed line), experimental (grey dashed line) and analytical (grey continuous line) results. The original picture, without the OpenFOAM curve, is reported from (Wimett, 1956). The smaller burst on the right is not simulated in the present work.

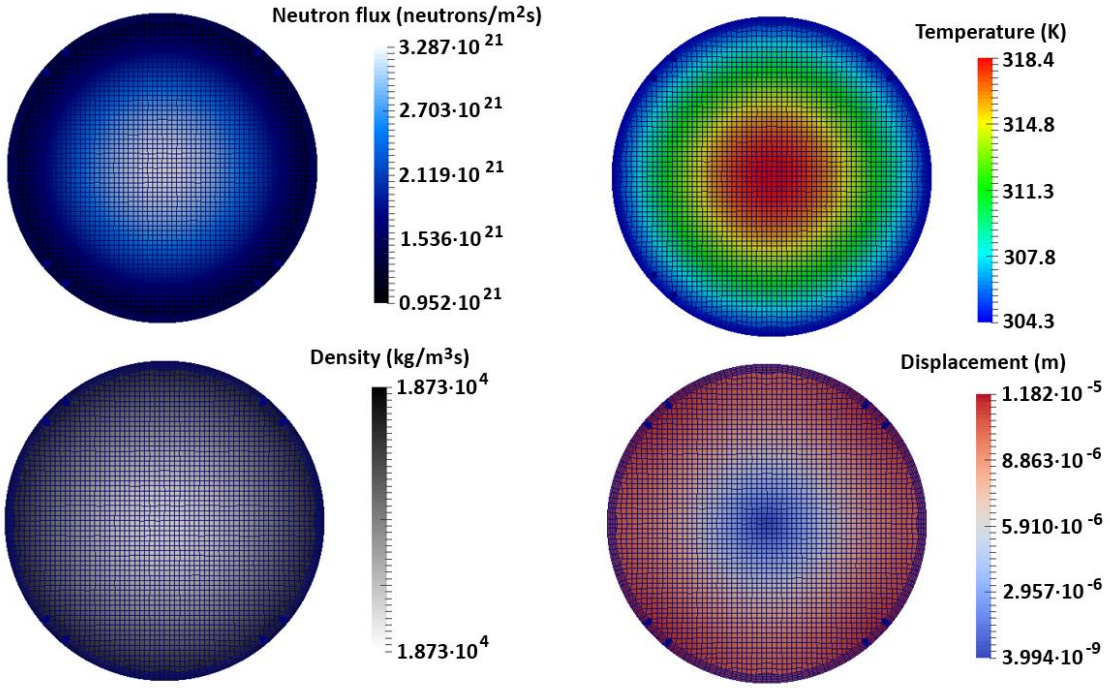

Figure 9. Neutron flux, temperature, density and displacement fields at fission rate peak.

4.1. Discussion of results

General good agreement is shown by the three curves (see Fig. 8), especially in the super-prompt-critical region, where the power increases, at the maximum, where the initial reactivity insertion is compensated by the negative thermal expansion feedback, and in the first part of the decreasing tail. At lower fission rates, the experimental data show a discrepancy with respect to the theoretical and the numerical results. This behavior was also observed by (Aufiero et al., 2015), by using a coupling between the continuous energy Monte Carlo code Serpent 2 and a linear thermo-elastic solver implemented in OpenFOAM, featuring a Lagrangian dynamic mesh (see Fig. 10).

As shown by Fig. 10, the Monte Carlo results are coincident with the theoretical one, while the experimental data depart from the other two curves about 0.1 millisecond after the peak and at a fission rate of about $4 \cdot 10^{18}$ fissions per second, in perfect agreement with the results shown in Fig. 8.

This suggests that the observed departure of the experimental curve is not dependent on the specific neutronics model, since the same results are obtained with completely different approaches (a discrete energy deterministic transport solver, a continuous energy Monte Carlo code and analytical point kinetics calculations). This aspect is discussed in detail by (Wimett, 1956) and can be imputed to neutron backscattering from the surrounding environment. Since the surrounding geometry is not known by the authors, this effect cannot be accounted for in the model.

Besides this discrepancy at the end of the transient, the burst is correctly reproduced by the solver. Considering that the initial reactivity is only 32 pcm above prompt-critical, that the fission rate increases by three order of magnitude in a few tenths of millisecond and that the relative volume variation of the sphere is as low as 0.05%, catching the coupling between neutronics and thermal mechanics is not trivial. Hence, the considered case study constitutes a severe benchmark for the proposed model. In particular, the outcome of this analysis constitutes a remarkable verification not only of the accuracy of the neutronics solver, but also of the capability of the moving mesh to describe the coupling between neutronics and geometry deformation. Indeed, thermal expansion is the only reactivity feedback mechanism considered in the simulation, since the Doppler effect is neglected. Consequently, the 0.05% volume variation, albeit small, is fundamental in determining the transient dynamics. In this regard, it is recalled that Aufiero et al. (2015) also employed a moving mesh to describe geometry deformations, while the analytical calculations are based on a negative reactivity coefficient approximating the thermal expansion effect – for details, see (Wimett, 1956). Therefore, modelling this feedback mechanism with accuracy is necessary to correctly describe the burst.

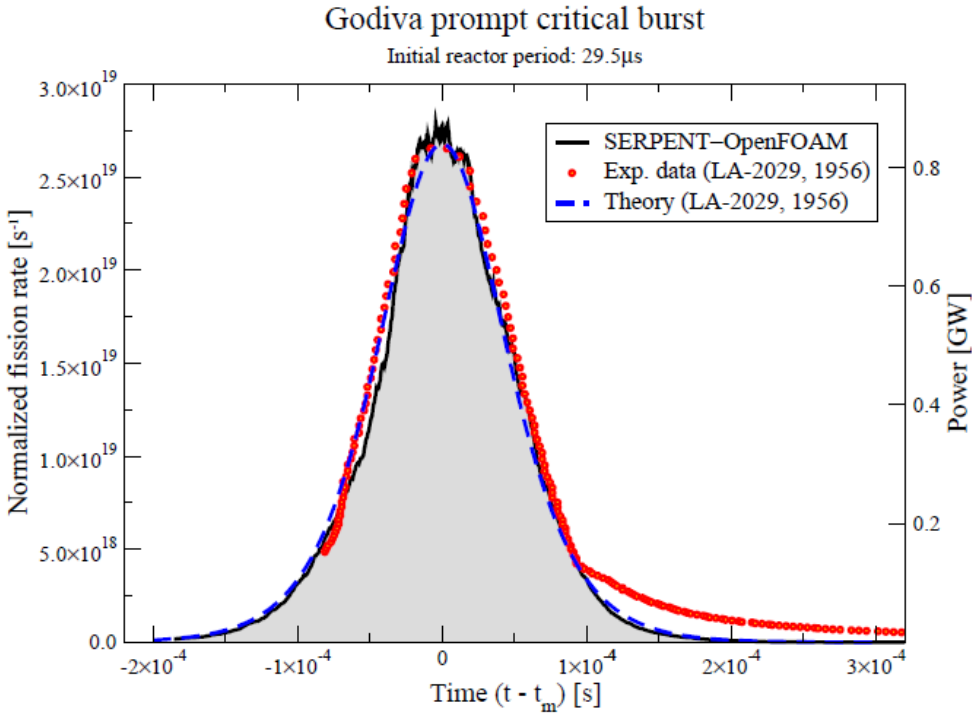

Figure 10. Monte Carlo, experimental and theoretical fission rates for the 29.5 μs burst. This picture is reported from (Aufiero et al., 2015).

5. COUPLING BETWEEN THE NEUTRONICS AND THE SHOCK PHYSICS MODULES

For demonstration purposes, two simple test cases are selected to show the multi-physics coupling between shockwave propagation and neutronics. As mentioned above, the study of shock imploding fissile bodies is of interest in many applications, especially in the subcritical experiments and nuclear criticality safety areas. Again, it is stressed that the considered case studies are not representative of real-life scenarios, as the purpose of this work is to present the model development and its capabilities. Both the test cases are treated using a Lagrangian point of view, while the improvements offered by an ALE approach will be discussed in Section 6. For simplicity, one-group cross sections are adopted for the estimation of the neutron flux.

The cases are selected to show:

1. the multiphysics coupling between neutronics and shockwave propagation;
2. the capability of the solver to reproduce typical shock physics phenomena, such as the interaction between two crossing shocks and the amplification of a converging shockwave;
3. the capability of the solver to deal with both subcritical and supercritical events.

The first case study consists of a 1D metallic uranium infinite slab, enriched at 90% in ^{235}U, with 6.5 cm thickness. A 30 GPa pressure step is applied at both sides of the slab at $t = 0$. The initial multiplication factor of the system, evaluated with the power iteration routine implemented into the solver, has a value of $k_{eff} = 0.98329$. The resulting pressure and fission rate profiles for $t = 6\ \mu s$ and $t = 12\ \mu s$ are shown in Fig. 11. In addition, the deformation of the mesh and the pressure and fission rate fields are presented in Fig. 12.

The shape of the two superimposing shocks is reflected in the fission rate profile, clearly showing the coupling between the two physics. The fission rate increases in correspondence of the shock front, where density is higher. However, the multiplication factor doesn't change significantly during the transient (when maximum compression is achieved, $k_{eff} = 0.98335$), meaning that the system remains subcritical and that the global neutron population is not increasing. In fact, due to the 1D slab geometry, the external surface is not reduced by the shock compression. In addition, the density increase, which tends to reduce neutron leakages, is counterbalanced by the thickness decrease, which has the opposite effect. Consequently, reactivity is nearly unaffected by the implosion. In other words, if the system is subcritical before compression, it also remains subcritical after the implosion.

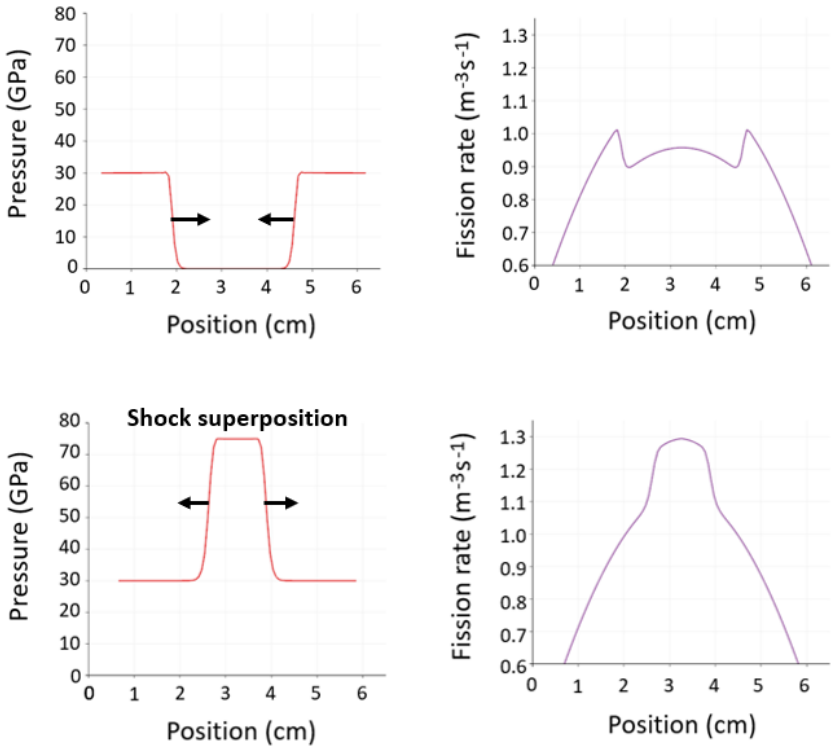

Figure 11. Pressure and fission rate profiles in the slab at $t = 6\ \mu s$ (top) and $t = 12\ \mu s$ (bottom).

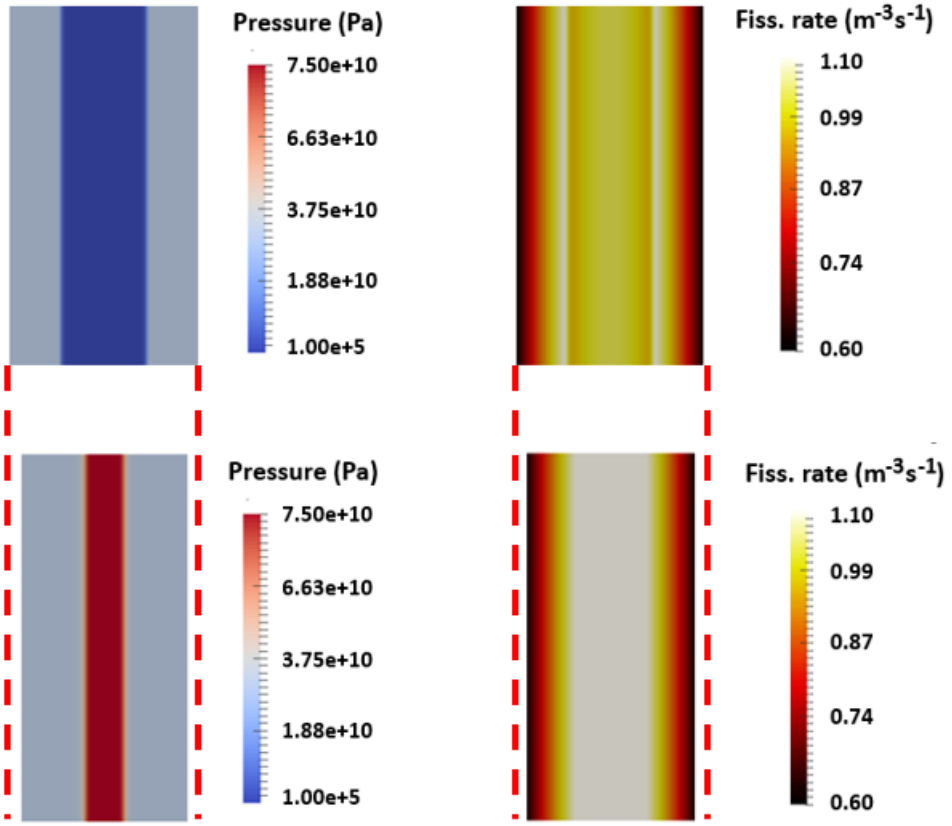

Figure 12. Pressure and fission rate fields in the slab at $t = 6\ \mu s$ (top) and $t = 12\ \mu s$ (bottom).

The second case study consists of a metallic uranium infinite cylinder, with 6 cm radius and same enrichment of the 1D slab. The initial multiplication factor of this system is $k_{eff} = 0.97911$. At $t = 0$, a 30 GPa pressure step is applied to the lateral surface of the cylinder. The pressure and fission rate profiles at $t = 8\ \mu s$ and $t = 16\ \mu s$ are shown in Fig. 13. In addition, the deformation of the mesh and the pressure and fission rate fields are presented in Fig. 14. Note that the shock front pressure increases as the shockwave converges towards the axis of the cylinder.

Differently from the 1D slab, this case becomes strongly supercritical. The fission rate increases of 24 decades between $t = 8\ \mu s$ and $t = 16\ \mu s$. In particular, at $t = 16\ \mu s$, the multiplication factor, evaluated with the power iteration routine implemented in the neutronics module, is $k_{eff} = 1.06520$. In fact, while in the 1D slab the surface area does not change with compression, in the cylinder case the external surface is significantly reduced by the shock implosion. Consequently, there are now two effects that decrease neutron leakages (the surface reduction and the material density increase) and only one that magnifies them (the diameter decrease). This leads to an overall reduction of neutron leakages and, as a consequence, to a strong reactivity increase.

Hence, even if the surface pressure is the same as the slab and the initial reactivity is similar, completely different transients are observed following dynamic compression, due to the different shapes of the two systems.

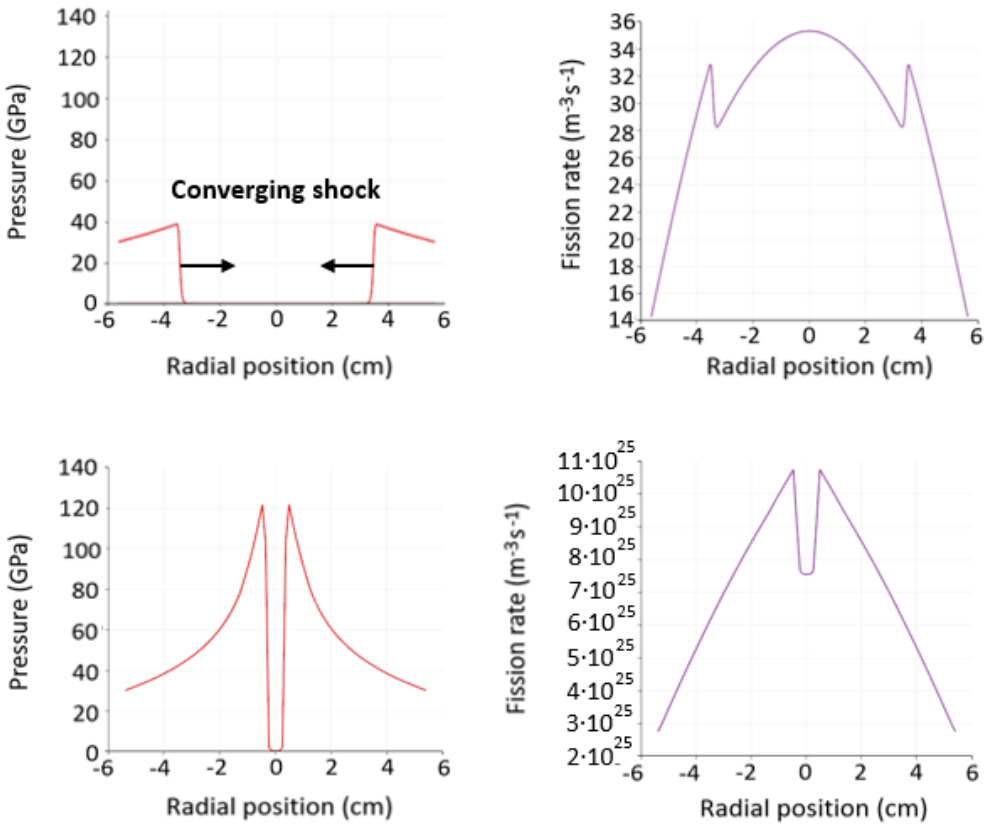

Figure 13. Pressure and fission rate profiles in the cylinder at $t = 8\ \mu s$ (left) and $t = 16\ \mu s$ (right).

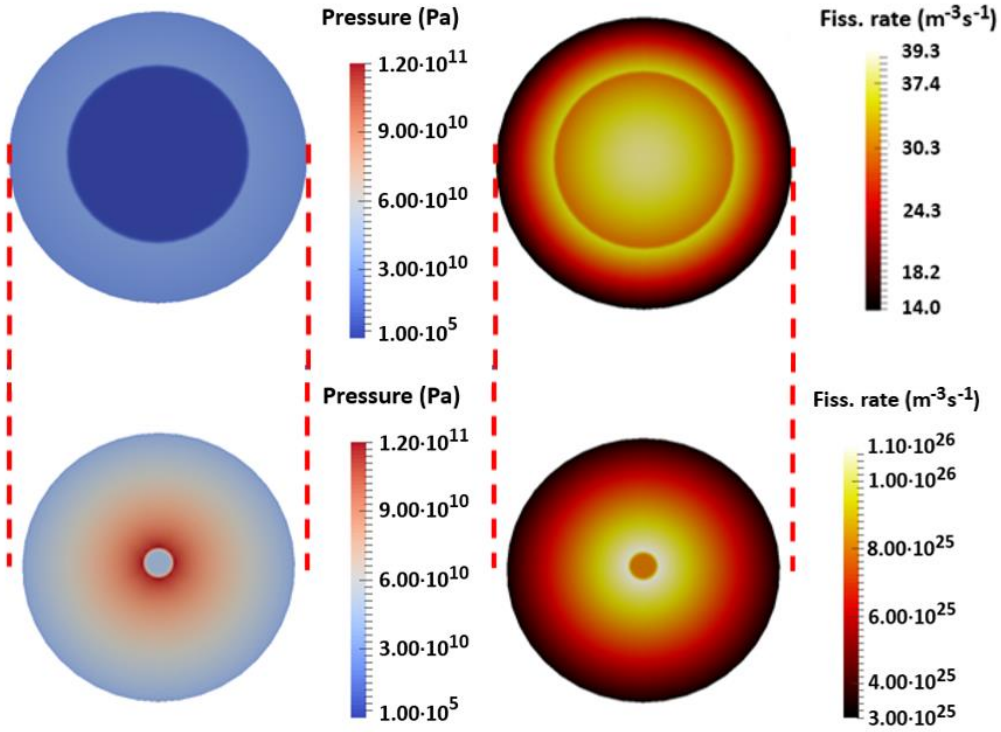

Figure 14. Pressure and fission rate fields in the cylinder at $t = 8\ \mu s$ (top) and $t = 16\ \mu s$ (bottom).

6. ALE ALGORITHM FOR COUPLED NEUTRONICS AND SHOCK PHYSICS PROBLEMS

In the previous sections, a Lagrangian point of view has been adopted for all the considered case studies. However, the governing equation of the thermal-mechanics model are written in an Arbitrary Lagrangian Eulerian formulation (see Section 2.1). In ALE methods, the mesh is displaced by using an arbitrary velocity, suitably chosen in order to avoid mesh distortion and tangling problems that are typical of Lagrangian approaches, limiting at the same time the interface smearing issues usually observed with Eulerian methods. Many algorithms are available in literature to determine the arbitrary mesh velocity (see, e.g., Barlow at al., 2016). This section aims at presenting a new ALE algorithm, specifically developed for the numerical simulation of shockwave compression of fissile materials.

The Lagrangian simulation of the cylinder implosion shown in Section 5 blows up just after $t = 16\ \mu s$. In fact, when the shockwave converges to the axis, mesh cells near the cylinder center begin to tangle due to the very high pressure. At the same time, the mesh quality is preserved near the boundary, where pressure is lower (see Fig. 13). In the light of this, a Eulerian point of view is required in the central part of the domain, while a Lagrangian point of view is preferable in the peripheral region. Indeed, the Eulerian approach, characterized by a fixed mesh, can avoid tangling problems where pressure is higher. On the other hand, the Lagrangian approach can ensure a better accuracy at describing boundary deformations (which is necessary to correctly estimate neutron leakages and reactivity in turn), being at the same time affordable due to the lower pressure values. Note that the above principle holds true not only for cylinders, but also for imploding bodies of different shapes, such as a plutonium or uranium spheres compressed by radial explosive charges.

Therefore, an ALE algorithm is desired that employs a Lagrangian approach near the boundary and a more Eulerian approach in the center of the mesh. In this regard, the neutron flux, which is lower near the system surface and higher in the center, can be identified as a potential criterion to switch from Lagrangian to Eulerian coordinates. In more details, where the flux is low (i.e., near the surface) a Lagrangian approach can be used, while a more Eulerian approach is preferable where the flux is high (i.e., in the center of the domain). Starting from this idea, which is schematized in Fig. 15, a new ALE algorithm is developed, suitable to study the shock implosion of solid fissile materials (Cervi and Cammi, 2019a).

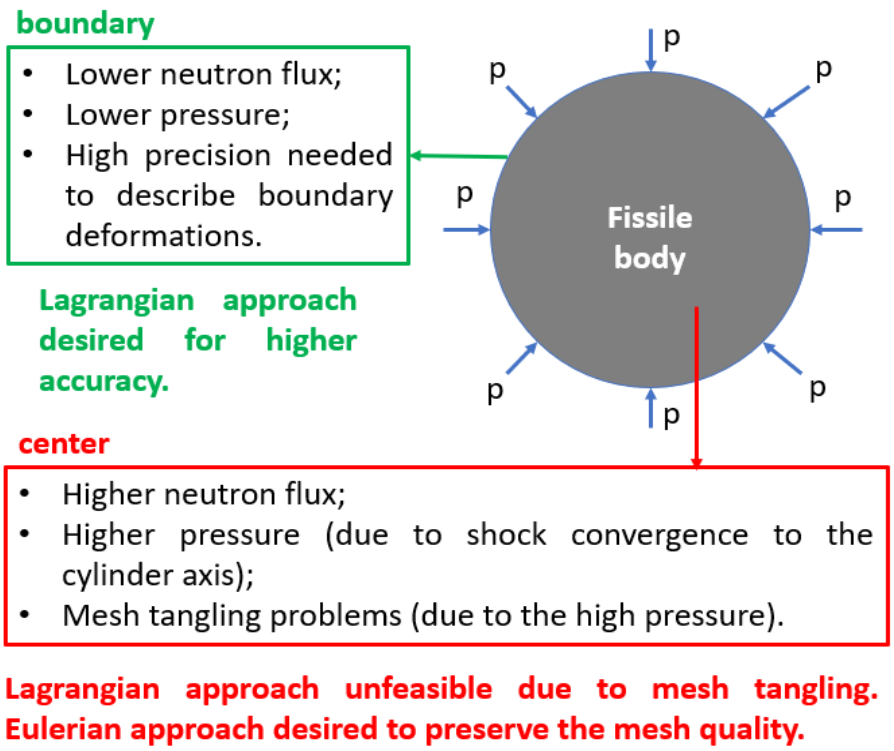

Figure 15. Schematic view of thee imploding cylinder and desired approaches to describe the shockwave propagation towards its axis.

The mathematical implementation of the proposed algorithm is now illustrated. Firstly, a function f_{ALE} is introduced, which is linked to the neutron flux by obeying to a neutron-diffusion-like equation:

$$\nabla \cdot D\nabla f_{ALE} - \Sigma_a f_{ALE} + \bar{\nu}\Sigma_f \varphi_{total} = 0 \qquad \text{with } f_{ALE} = 0 \text{ at boundary} \tag{24}$$

Note that more accurate neutronics equations are not strictly required, since the aim of Eq. (24) is only to determine an approximated shape of the neutron flux, and not to give an accurate description of the system neutronics. For the latter purpose, the neutron transport models introduced in Section 2.2 and in Appendix A can be employed. For the same reason, distinction between different energy groups is not necessary and the time derivative can be omitted. It is important to observe that zero boundary conditions are imposed. Consequently, the total neutron flux φ_{total} must appear in the fission term of Eq. (24), in order to avoid an identically null solution.

Then, f_{ALE} is normalized with respect to its maximum value as follows:

$$F_{ALE} = \frac{f_{ALE}}{\max\left(f_{ALE}\right)} \tag{25}$$

According to Eq. (25) and to the zero boundary condition imposed to f_{ALE}, the value of the normalized function F_{ALE} is always between 0 and 1. In the light of this, F_{ALE} can be chosen as the criterion to switch between the Eulerian and Lagrangian approaches. In more details, this is achieved by defining the arbitrary mesh velocity $\boldsymbol{w}$ as follows:

$$\boldsymbol{w} = \boldsymbol{u}(1 - F_{ALE}) \tag{26}$$

According to Eq. (26), if $F_{ALE} = 0$ (i.e., at the boundary), $\boldsymbol{w} = \boldsymbol{u}$ and the point of view is purely Lagrangian. On the other hand, if $F_{ALE} = 1$ (i.e., at the center), $\boldsymbol{w} = 0$ and the point of view becomes Eulerian. However, a transition from a purely Lagrangian to a purely Eulerian approach is not only unnecessary, but can still lead to numerical problems (due to tangling issues in the transition region). For this reason, Eq. (26) is slightly modified by introducing an under-relaxation coefficient which multiplies F_{ALE}:

$$\boldsymbol{w} = \boldsymbol{u}(1 - r_{ALE}F_{ALE}) \quad \text{with } r_{ALE} \in [0, 1] \tag{27}$$

Due to r_{ALE}, the center of the domain is not treated with purely Eulerian coordinates, but with a mixed Lagrangian and Eulerian approach. By this way, the transition between the two points of view is more gradual, compared to Eq. (26) and mesh tangling can be avoided in the entire domain. The under-relaxation coefficient r_{ALE} should be set to the minimum value that avoids mesh tangling, without, at the same time, departing too much from the more accurate Lagrangian point of view. For the case of interest, this can be achieved by choosing $r_{ALE} \in [0.2, 0.5]$. Using this range of values, the authors repeated the validation presented in Section 3, verifying that results are not affected by the adoption of this ALE algorithm.

6.1. Arbitrary Lagrangian-Eulerian vs. purely Lagrangian approaches

6.1.1. Cylinder case studies

The ALE algorithm described in the previous section is now applied to the imploding cylinder case, in order to assess its advantages compared to a purely Lagrangian approach. As mentioned in Section 6, the Lagrangian simulation of the imploding cylinder runs until $t = 16\ \mu s$, then it blows up due to mesh tangling at the axis. The cylinder simulation is now repeated using the proposed ALE algorithm, setting $r_{ALE} = 0.2$.

A first simulation is carried out considering a 3 cm radius cylinder (initial $k_{eff} = 0.56650$), so that the system remains subcritical during the implosion and its deformation is only determined by the surface pressure and the material properties (and not by the thermal expansion due to a supercritical fission power burst). On the other hand, a second simulation is carried out with a 6 cm radius cylinder (initial $k_{eff} = 0.97911$). In this case, the system is made supercritical by the shock implosion and the fission power heating introduces a further pressure contribution, as shown later in this section. In both cases, a 90% ^{235}U enrichment is assumed.

The time evolution of the pressure profile in the smaller cylinder, using the ALE approach, is shown in Fig. 16. At the beginning of the implosion, the shockwave converges towards the center of the cylinder. Then, at $t = 8.4\ \mu s$, the shock front reaches the axis and pressure abruptly increases, up to a value of about 18 Mbar. Afterwards, the shockwave returns towards the cylinder surface, pressure decreases and the cylinder expands.

On the other hand, the pressure profile in the bigger cylinder is shown in Fig. 17. Minimum volume is achieved at $t = 16.8\ \mu s$, when the shock converges at the axis, and pressure reaches 65 Mbar. As already shown in Section 5, the shock compression strongly increases reactivity making the system supercritical. The fission energy release leads to a bell-shaped pressure profile, which is superimposed to the pressure peak produced by shock convergence. Afterwards, due to thermal expansion, the cylinder returns to its original diameter at $t = 16.95\ \mu s$ (i.e., 0.15 μs after shock convergence). It's worth noting that, despite the rapid expansion, the mesh is not blown apart. During this short time interval, pressure continues to grow despite the volume increase, since fission reactions are still heating the system. In particular, at $t = 16.95\ \mu s$, pressure reaches a peak value of about 103 Mbar. As a term of comparison, the Chapman-Jouguet pressures of typical high-performance explosives are between 100 and 400 kbar (Coleburn, 1964; Thompson, 1972).

Conversely, due to mesh tangling, purely Lagrangian simulations of both the cases blow up just before shock convergence, at $t = 8.00\ \mu s$ for the smaller cylinder and at $t = 16.00\ \mu s$ for the bigger one. These results point out that the proposed ALE algorithm is highly effective in avoiding mesh tangling, allowing to simulate much higher pressures compared to purely Lagrangian approaches. Since with the ALE approach simulations do not blow up at shock convergence, the subsequent expansion of the cylinder can also be studied.

Note that the Lagrangian and the ALE pressure profiles are superimposed until mesh tangling occurs. Therefore, only the ALE results are plotted for the sake of readability.

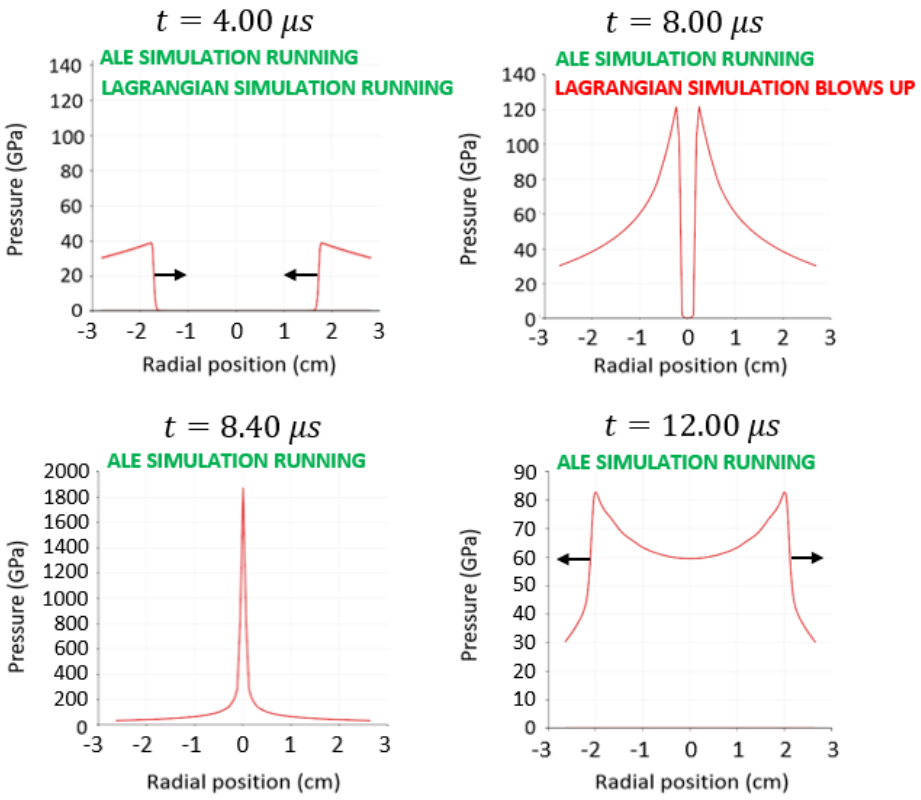

Figure 16. Shock implosion transient with $r_{ALE} = 0.2$ in the subcritical cylinder.

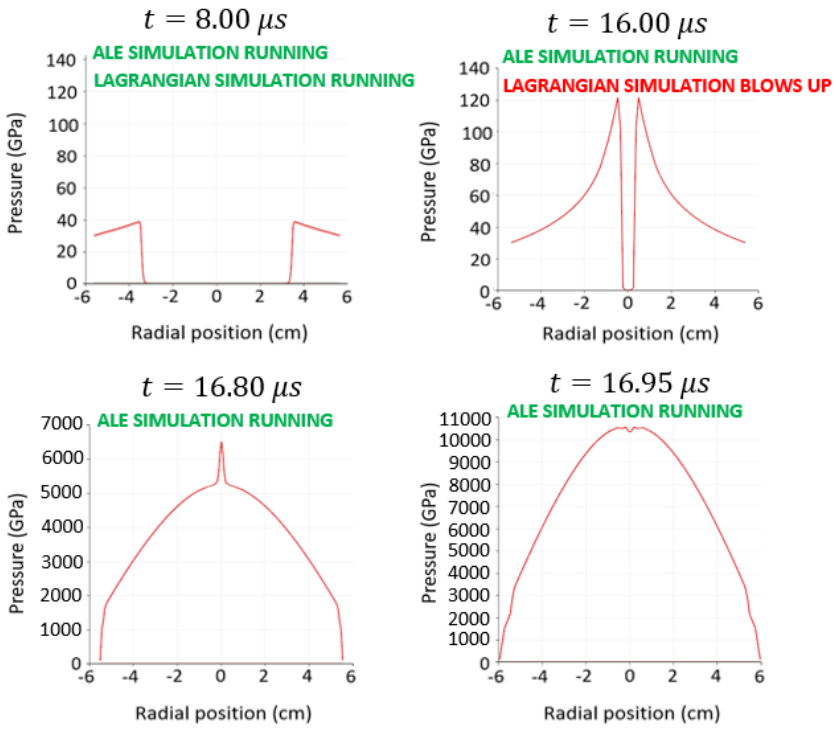

Figure 17. Shock implosion transient with $r_{ALE} = 0.2$ in the supercritical cylinder.

To emphasize the advantage of the proposed ALE algorithm, the time evolution of the cell Jacobian is now analysed. To this purpose, it is recalled that the deformation of a mesh cell from a time step to the following one is related to the cell Jacobian according to the following relation:

$$V_{cell}(t + \Delta t) = J_{cell}(t) V_{cell}(t) \tag{28}$$

Consequently, the Jacobian is a good indicator of mesh tangling issues, as a negative value means that the corresponding cell volume is becoming negative in the following time step. The time-behavior of the minimum Jacobian over the entire computational domain is plotted in Figs. (18) and (19) for the smaller and the bigger cylinder, respectively. Note that the minimum Jacobian over all the cells is selected because it is the first to become negative in case of mesh tangling. It is important to understand that the minimum Jacobian does not belong to a specific cell, but moves from a cell to another as time advances and the shockwave propagates through the medium.

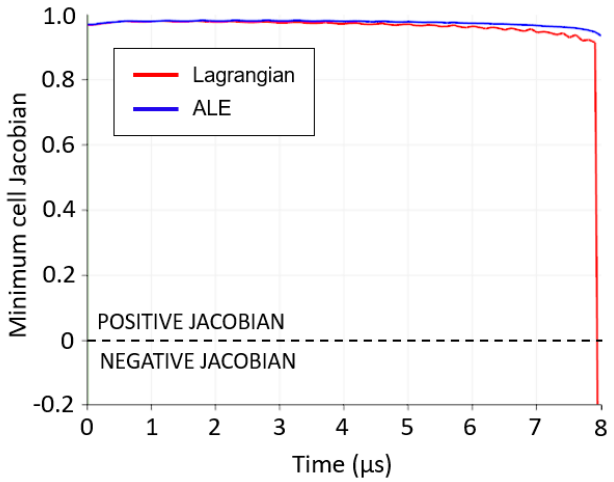

Figure 18. Minimum cell Jacobian (3 cm radius cylinder). The y-axis range is limited between -0.2 and 1.0 for the sake of readability.

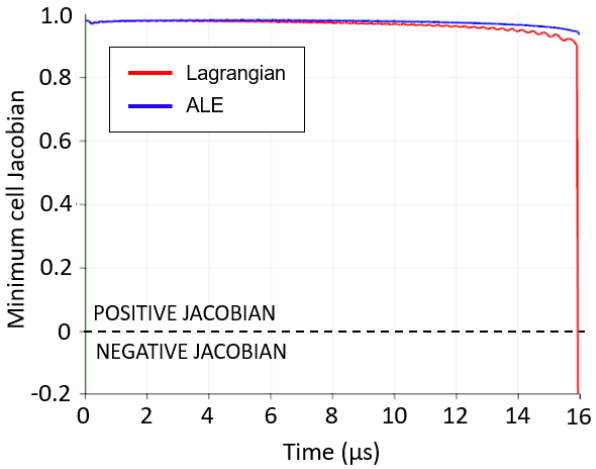

Figure 19. Minimum cell Jacobian (6 cm radius cylinder). The y-axis range is limited between -0.2 and 1.0 for the sake of readability.

In both cases, the Lagrangian simulation Jacobians decrease faster, compared to the ALE ones, and become negative when mesh distortion occurs (i.e., at $t = 8.00\ \mu s$ and $t = 16.00\ \mu s$). On the other hand, the ALE simulation Jacobians remain positive, pointing out that the mesh quality is preserved.

6.1.2. Slab case studies

Two additional case studies are presented in this section, to test the ALE algorithm on a different geometry:

- A uranium slab with 40 cm thickness, compressed from both sides with a 70 GPa pressure;
- A plutonium slab with 40 cm thickness, compressed from both sides with a 50 GPa pressure;

The corresponding pressure profiles are presented in Figs. (20) and (21), while the minimum Jacobian vs. time is shown in Figs. (22) and (23), respectively. Again, the Lagrangian simulations blow up when the left and right shockwaves meet at the slab center, while the ALE simulations can reproduce the shock superposition. Consistently, the Lagrangian simulation Jacobians become negative when mesh tangling occurs, while the ALE simulation Jacobians remain positive.

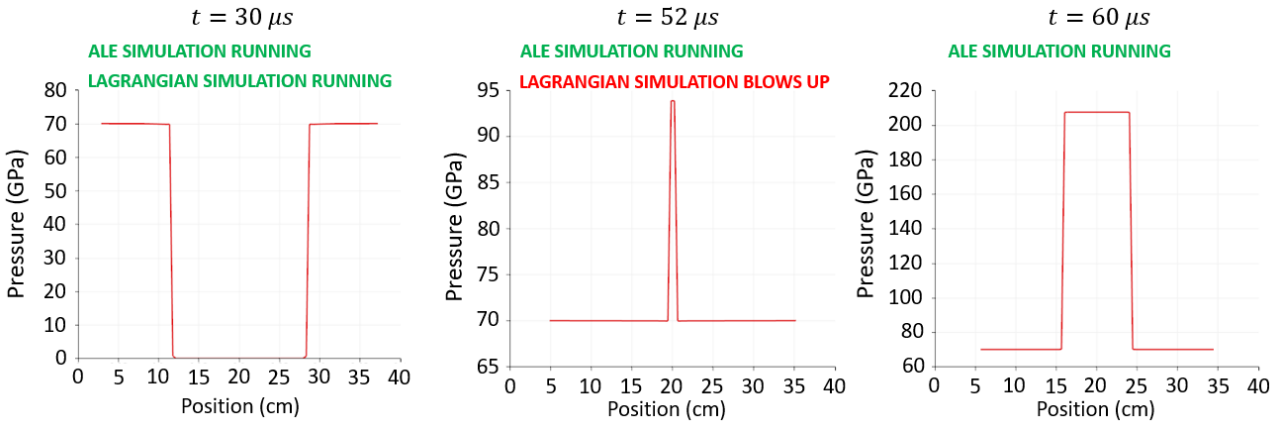

Figure 20. Shock compression transient with $r_{ALE} = 0.2$ in the uranium slab.

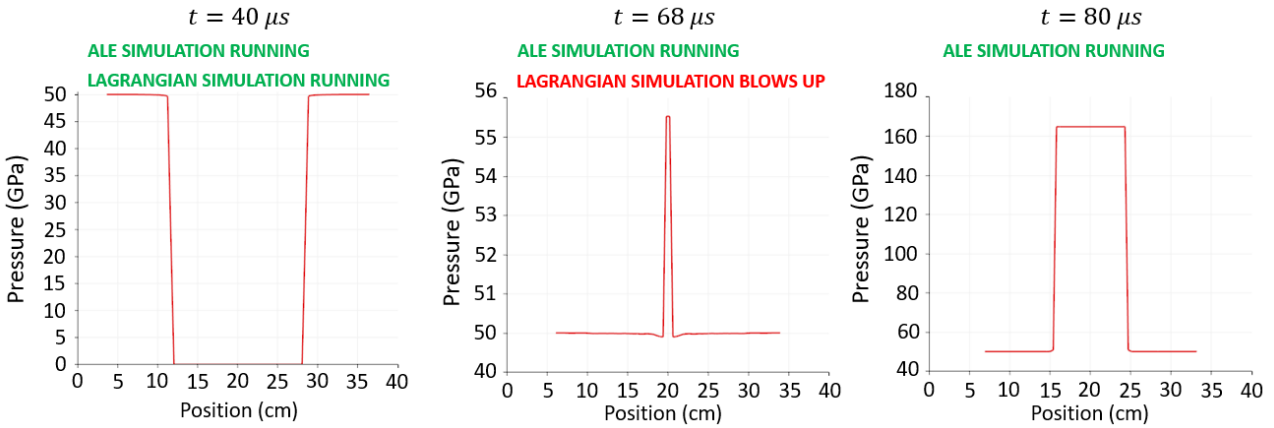

Figure 21. Shock compression transient with $r_{ALE} = 0.2$ in the plutonium slab.

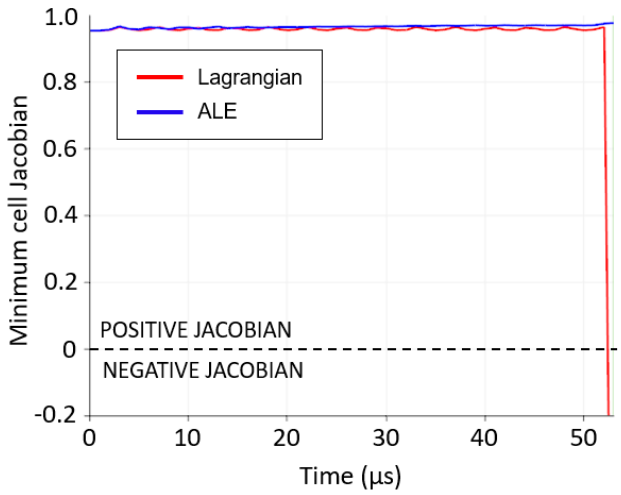

Figure 22. Minimum cell Jacobian (uranium slab). The y-axis range is limited between -0.2 and 1.0 for the sake of readability.

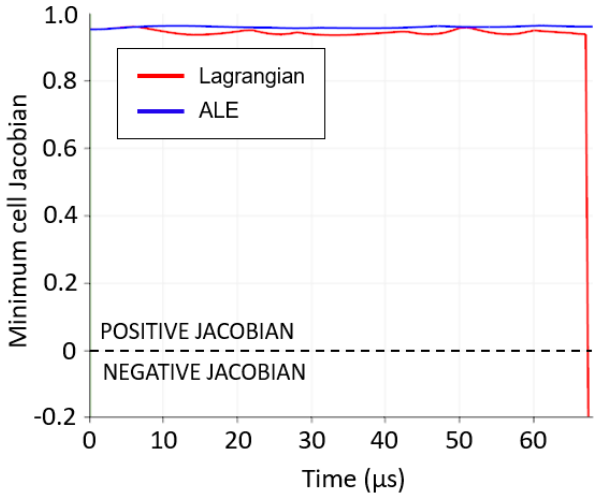

Figure 23. Minimum cell Jacobian (plutonium slab). The y-axis range is limited between -0.2 and 1.0 for the sake of readability.

7. CONCLUSIONS

In this work, a new multiphysics model for the analysis of shockwave compression of solid fissile materials is presented. The shock physics model is validated against experimental Hugoniot curves of different metallic materials, while the neutronics model and its coupling to thermal-mechanics is validated against a Godiva super-prompt-critical burst.

Then, the solver is tested on two simple case studies - a slab and a cylinder, both imploded by applying an external pressure - highlighting the effect of geometry on the reactivity response. In particular, even if the two systems have similar initial multiplication factors and the same pressure is applied to their surfaces, the slab remain subcritical, while the cylinder becomes highly supercritical. In fact, the slab external surface is not modified by the shock compression, while the cylinder surface is strongly reduced during the implosion, decreasing neutron leakages and increasing reactivity in turn. Finally, a new ALE algorithm, specifically developed for coupled neutronics-shock physics problems, is presented, showing significant improvements compared to a purely Lagrangian approach.

In the light of these results, the proposed model is a promising tool for the analysis of shock imploding multiplying systems. In particular, this solver can be useful to design subcritical uranium and plutonium experiments and to assess their safety from a criticality point of view. More in general, the model can find application in the study of reactivity accidents initiated by strongly energetic events such as chemical explosions. In this perspective, the development and validation of detonation models is planned as a future step, in order to explicitly simulate the explosive charges that wrap the fissile samples.

Furthermore, thanks to the multi-material formulation of the governing equation, the present model can be used to simulate high-velocity impact events. This capability is currently being tested with promising results on different case studies, such as projectile-wall impacts and collisions between fissile bodies. In this regard, the implementation of additional constitutive relations - e.g., the Johnson-Cook failure model (Johnson and Cook, 1985) - may represent a substantial improvement, paving the way to more detailed simulations of complex phenomena such as spall fracture.

APPENDIX A. Development and preliminary verification of an S_N neutron transport model

The SP_3 model adopted in this work showed an excellent behavior in the Godiva test case (Section 4) and was successfully verified for nuclear reactor application in (Cervi et al., 2019b; Cervi et al., 2019c). However, due to its approximations (Brantley and Larsen, 2000), simplified P_N approaches still constitute a compromise between neutron diffusion and neutron transport, not only in terms of runtimes but also of accuracy. Therefore, the SP_3 model may not be the best approach to study small, strongly leakage-dominated geometries such as the ones that characterize plutonium subcritical experiments. To address this issue, a discrete ordinate (S_N) model is implemented into the multiphysics solver (Cervi and Cammi, 2019b).

For a given neutron energy group ei and a free-flight direction di, the neutron transport equation can be formulated as follows:

$$\frac{1}{v_{ei}}\frac{\partial \varphi_{ei,di}}{\partial t} + \nabla \cdot \left[(v_{ei}\boldsymbol{\Omega}_{di} - \boldsymbol{w}) \cdot n_{ei,di}\right] + \Sigma_{tot,ei}\varphi_{ei,di} = S_{f,ei,di} + S_{s,ei,di} + S_{d,ei,di} + Q_{ei,di} \tag{A.1}$$

where the arbitrary mesh velocity $\boldsymbol{w}$ appears in the divergence term, due to the ALE formulation of the model. The effect of the solid particle motion on neutron flux (Baker et al., 2015) is not considered for simplicity.

Both the number of energy groups and of flight directions can be arbitrarily selected by the user. The terms $S_{f,ei,di}$, $S_{s,ei,di}$ and $S_{d,ei,di}$ represent the fission source, the scattering neutrons and the delayed neutron source, respectively, and they are defined as follows:

$$S_{f,ei,di} = \sum_{ei',di'} \varphi_{ei',di'} w_{di'} \left[\nu_{ei'} \Sigma_{f,ei'} \chi_{p,ei}(1-\beta_{tot})\right] \tag{A.2}$$

$$S_{s,ei,di} = \sum_{ei',di',l} P_l(\boldsymbol{\Omega}_{di} \cdot \boldsymbol{\Omega}_{di'})(2l+1)\, \Sigma_{sl,ei'\to ei} \varphi_{ei',di'} w_{di'} \tag{A.3}$$

$$S_{d,ei,di} = \sum_k \lambda_k c_k w_{di} \tag{A.4}$$

where w_{di} is the weight of the direction di. As for the SP_3 model, precursor densities are evaluated with Eq. (23).

A source $Q_{ei,di}$ can also be considered for each energy group and direction combination. Its intensity and position can be defined by the user. If the neutron source is placed outside the computational domain, it can be accounted for as a boundary condition. This can be of interest for subcritical experiments in which the fissile sample is irradiated by an external source (Hutterer, 2017).

To verify the new model, 95% enriched uranium cubes of different dimensions are adopted as case studies. The multiplication factor of these cubes is evaluated using both the SP_3 and the S_N modules and the results are compared to continuous energy Monte Carlo simulation. An S_6 angular discretization (i.e., 48 free-flight directions) and four energy groups (with cutoffs at 1, 2 and 3 MeV) are adopted, considering anisotropic scattering up to the seventh order. The directions and weights adopted in this work are based on the level symmetric quadrature sets given in (Lewis and Miller, 1984). Four energy groups are also selected for the SP_3 solver. On the other hand, Monte Carlo simulations are carried out using 100 million active neutron histories (10,000 cycles of 10,000 particles, plus 1000 inactive cycles to ensure fission source convergence).

The aim of this verification is to assess the capability of the two neutronics models to correctly predict reactivity in small systems, where neutron leakages are dominant and simpler models such as the SP_3 equations may have significant limitations. Results are listed in Tabs. A.I and A.II.

Table A.I. S_N vs. Monte Carlo results.

Cube edge (cm)	k_{eff} S_N	k_{eff} MC	Error (pcm)
16	1.07376	1.07424 ± 0.00009	-48
8	0.58075	0.57992 ± 0.00007	+83
4	0.29227	0.29193 ± 0.00004	+34
2	0.14519	0.14519 ± 0.00003	0
1	0.07222	0.07226 ± 0.00002	-4

Table A.II. SP_3 vs. Monte Carlo results.

Cube edge (cm)	k_{eff} SP_3	k_{eff} MC	Error (pcm)
16	1.06767	1.07424 ± 0.00009	-657
8	0.58567	0.57992 ± 0.00007	+575
4	0.29362	0.29193 ± 0.00004	+169
2	0.14352	0.14519 ± 0.00003	-167
1	0.07004	0.07226 ± 0.00002	-222

Even using a relatively low number of flight directions, the S_N model performs significantly better than the SP_3 one, always reducing the error with respect to Monte Carlo simulation well below 100 pcm. This improvement can be useful for a more accurate simulation of subcritical plutonium experiments, where small

dimension and strong shock-induced density gradients may pose several limits on the SP_3 approach. The application of this model to shock-implosion problems has been preliminary tested in (Cervi and Cammi, 2019b). However, the development of efficient acceleration techniques or reduced order methods is required to decrease runtimes (which are about 30 times larger compared to the SP_3 model). In addition, it is well known that discrete-ordinate approaches can be affected by ray-effect issues due to the finite number of angular directions. Therefore, suitable mitigation strategies should be adopted to address this problem as well (see, e.g., Camminady et al., 2019).

In principle, any neutronics model could be coupled with the proposed shock physics solver. For example, Aufiero et al. (2015) proposed a coupling between the Monte Carlo code Serpent (Leppänen et al., 2015) and a linear thermo-elastic solver featuring a Lagrangian moving mesh. Even though such a model is only suitable to describe small deformations, the same approach could be extended to the simulation of large-strain and shockwave problems.

BIBLIOGRAPHY

Aufiero, M., Fiorina, C., Laureau, A., Rubiolo, P., 2015. Serpent-OpenFOAM coupling in transient mode: simulation of a Godiva prompt critical burst, ANS MC2015 Joint International Conference on Mathematics and Computation (M&C), Supercomputing in Nuclear Applications (SNA) and Monte Carlo (MC) Method, April 19-23 2015, Nashville, TN, USA.

Baker R.S., Dahl, J.A., Fichtl, E.J., Morel, J.E., 2015. Neutron transport in Eulerian coordinates with bulk material motion, Nuclear Engineering and Design 295, 667-673.

Barlow, A.J., Maire, P.-H., Rider, W.J., Rieben, R.N., Shashkov, M.J., 2016. Arbitrary Lagrangian-Eulerian methods for modelling high speed compressible multimaterial flows, Journal of Computational Physics 322, 603-665.

Bell, G.I., Glasstone, S., 1970. Nuclear Reactor Theory, Van Nostrand Reinhold Company, New York.

Brandtley, P.S., Larsen, E.W., 2000. The simplified P3 approximation, Nuclear Science and Engineering 134, 1-21.

Camminady, T., Frank, M., Küpper, K., Kusch, J., 2019. Ray effect mitigation for the discrete ordinates method through quadrature rotation.

Cervi, E., Lorenzi, S., Cammi, A., Luzzi, L., 2017. An Euler-Euler multi-physics solver for the analysis of the helium bubbling system in the MSFR, NENE 2017 26th International Conference Nuclear Energy for New Europe, September 11-14, 2017, Bled, Slovenia.

Cervi, E., Lorenzi, S., Cammi, A., Luzzi, L., 2018. Analysis of the effect of fuel compressibility on super-prompt-critical dynamics of the Molten Salt Fast Reactor. PHYSOR 2018 Reactor Physics paving the way towards more efficient systems, April 22-26 2018, Cancun, Mexico.

Cervi, E., Lorenzi, S., Luzzi, L., Cammi, A., 2018. Analysis of the void reactivity effect in the Molten Salt Fast Reactor: impact of the helium bubbling system. PHYTRA4 The Fourth International Conference on Physics and Technology of Reactors and Applications, September 17-19 2018, Marrakech, Morocco.

Cervi, E., Lorenzi, S., Luzzi, L., Cammi, A., 2018. An OpenFOAM solver for criticality safety assessment in dynamic compression events, Transactions of the American Nuclear Society 119, 855-858.

Cervi, E., Cammi, A., 2019. An Arbitrary Lagrangian Eulerian solver for shock imploding fissile materials, Transactions of the American Nuclear Society 121, 763-766. https://dx.doi.org/10.13182/T31112

Cervi, E., Cammi, A., 2019. A Coupled Neutronics Shock Physics Solver: Implementation of an SN Neutron Transport Module, Transactions of the American Nuclear Society 121, 767-770. https://dx.doi.org/10.13182/T31114

Cervi, E., Lorenzi, S., Cammi, A., Luzzi, L., 2019. Development of a multiphysics model for the study of fuel compressibility effects in the Molten Salt Fast Reactor, Chemical Engineering Science 193, 379-393. https://doi.org/10.1016/j.ces.2018.09.025

Cervi, E., Lorenzi, S., Cammi, A., Luzzi, L., 2019. Development of an SP3 neutron transport solver for the analysis of the Molten Salt Fast Reactor, Nuclear Engineering and Design 346, 209-219. https://doi.org/10.1016/j.nucengdes.2019.03.001

Cervi, E., Lorenzi, S., Luzzi, L., Cammi, A., 2019. Multiphysics analysis of the MSFR helium bubbling system: A comparison between neutron diffusion, SP3 neutron transport and Monte Carlo approaches, Annals of Nuclear Energy 132, 227-235. https://doi.org/10.1016/j.anucene.2019.04.029

Coleburn, N.L., 1964, Chapman-Jouguet pressures of several pure and mixed explosives, Naval Ordnance Laboratory, White Oak, MD, USA.

Davison, L., 2008. Fundamentals of Shock Wave Propagation in Solids, Springer-Verlag Berlin Heidelberg.

Dillingham, C., 2016. Do Subcritical Experiments Help?, National Security Science, available at: https://www.lanl.gov/discover/publications/national-security-science/2016-december/do-subcritical.php

DOE Technical Standard, 2017. Preparing critical safety evaluations at department of energy nonreactor facilities.

Donea, J., Huerta, A., Ponthot, J.-Ph., Rodríguez-Ferran, A., 2004. Arbitrary Lagrangian-Eulerian Methods, Encyclopedia of Computational Mechanics, Wiley Online Library.

Fung, Y.C., Tong, P., 2001. Classical and Computational Solid Mechanics ,World Scientific Publishing Co. Pte. Ltd., Singapore.

Grodzka P.G., 1967. Gruneisen parameter study, Lockheed Missiles and Space Company.

Hirt, C.W., Amsden, A.A., Cook, J.L., 1974. An arbitrary Lagrangian-Eulerian computing method for all flow speeds, Journal of Computational Physics 14, 227-253.

Hutterer, E., 2017. The bomb without the boom, available at: https://www.lanl.gov/discover/publications/1663/2017-october/bomb-without-boom.php

IAEA Safety Standards, 2014. Criticality Safety in the Handling of Fissile Material.

Isbell, W.M., Shipman, F.H., Jones, A.H., 1971. Hugoniot equation of state measurements for eleven materials to five Megabars, Materials & Structures Laboratory Manufactory Development, General Motor Corporation.

Johnson, G.R, Cook, W.H., 1985. Fracture characteristics of three metals subjected to various strains, strain rates, temperatures and pressures, Engineering Fracture Mechanics 21, 31-48.

Leppänen, J., Pusa, M., Viitanen, T., Valtavirta, V., Kaltiaisenaho, T., 2015. The Serpent Monte Carlo code: Status, development and application in 2013, Ann. Nucl. Energy 82, 142-150.

LeVeque, R., 2002. Finite Volume Methods for Hyperbolic Problems, Cambridge University Press, Cambridge.

Lewis, E.E., Miller, W.F., 1984. Computational methods of neutron transport, John Wiley & Sons, New York/Chichester/Brisbane/Toronto/Singapore.

Mahadevan, V.S., Ragusa, J.C., Mousseau, V.A., 2012. A verification exercise in multiphysics simulations for coupled reactor physics calculations, Progress in Nuclear Energy 55, 12-32.

McGlaun, J.M., Thompson, S.L., 1990. CTH: A three-dimensional shock wave physics code, International Journal of Impact Engineering 10, 351-360.

Moukalled, F., Mangani, L., Darwish, M., 2016. The Finite Volume Method in Computational Fluid Dynamics, Springer, New York.

OpenFOAM, 2013. OpenFOAM Documentation, available at http://www.openfoam.org/docs/.

Santamarina, A., Bernard, D., Blaise, P., Coste, M., Courcelle, A., Huynh, T.D., Jouanne, C., Leconte, P., Litaize, O., Ruggiéri, J-M., Sérot, O., Tommasi, J., Vaglio, C., Vidal, J-F., 2009. The JEFF-3.1.1 Nuclear Data Library, JEFF Report 22, OECD/NEA.

Stacey, W. M., 2007. Nuclear Reactor Physics, Wiley-VCH, Weinheim.

Summers, R.M., Peery, J.S., Wong, M.W., Herten Jr., E.S., Trucano, T.G., Chhabildas, L.C., 1997. Recent progress in ALEGRA development and application to ballistic impacts, International Journal of Impact Engineering 20, 779-788.

Ragusa, J.C., Mahadevan, V.S., 2009. Consistent and accurate schemes for coupled neutronics thermal-hydraulics reactor analysis, Nuclear Engineering and Design 239, 566-579.

Robinson, A.C., Brunner, T.A., Carroll, S., Drake, R., Garasi, C.J., Gardiner, T., Haill, T., Hanshaw, H., Hensinger, D., Labreche, D., Lemke, R., Love, E., Luchini, C., Mosso, S., Niederhaus, J., Ober, C.C., Petney, S., Rider, W.J., Scovazzi, G., Strack, O.E., Summers, R., Trucano, T., Weirs, V.G., Wong, M., Voth, T., 2008. ALEGRA: An Arbitrary Lagrangian-Eulerian Multimaterial, Multiphysics Code, 46th AIAA Aerospace Sciences Meeting and Exhibit, January 7-10 2008, Reno, NV, USA.

Thompson, P.A., 1972. Compressible-fluid dynamics, McGraw Hill Book Company, New York.

Wimett, T.F., 1956. Time behavior of Godiva through prompt critical, LA-2029, Los Alamos National Laboratory.